Chapter 10
Signal Processing for Particle Detectors

V. Radeka

10.1 Introduction

This chapter covers the principles and basic limits of signal processing for detectors based on measurements of charge induced on predominantly capacitive electrodes. While this presents a very limited scope, it already includes a broad range of different detector technologies employed in experiments in several areas of science and in various imaging devices. Detector technologies of interest involve semiconductors, gas and liquid ionization media as well as photo detectors converting (scintillation light) into photo-electrons or ionization. One class of detectors not considered here are bolometric detectors (see Sect. 10.4).

The literature cited in this chapter is twofold: the textbooks, tutorials and review articles which may serve to provide a systematic introduction to the reader, and references to journal articles describing specific applications and technological solutions. The former, while very good and useful, are unfortunately few, the latter are only a small selection from the vast body of journal articles and conference records. The former are listed first [1–10], and the latter are cited along with the material presented in this chapter.

For many detectors, particularly very large scale detectors used at colliding beam machines in particle and nuclear physics, systems aspects require most of the attention in the design. In high precision measurements of energy, time arrival or position of the incident particle or photon the noise introduced in the measurement is of primary interest. Each area of science may impose greatly different requirements on various performance parameters of the detector and signal processing. A silicon pixel detector for particle tracking at a high luminosity collider requires very short

V. Radeka (✉)
Brookhaven National Laboratory, Upton, NY, USA
e-mail: radeka@bnl.gov

C. W. Fabjan, H. Schopper (eds.), *Particle Physics Reference Library*,
https://doi.org/10.1007/978-3-030-35318-6_10

pulse shaping (a few tens of nanoseconds) and it can tolerate a noise level of several hundred electrons rms. Consequently, a leakage (dark) current contributing shot noise may be 1 nA/cm^2 or more. A silicon detector for x-ray spectroscopy in photon science must be read out with a total noise of less than ten electrons rms with a shaping time of the order of 1 μs. This allows a leakage current of only ~10 pA/cm^2 or less. This chapter should enable the reader to evaluate the relations among such detector and readout parameters.

Signal processing for particle detectors rests on understanding of signal formation and of the sources of noise and their effects on measurement accuracy. Signal formation in detectors is based on electrostatics and it is calculated relatively easily starting from the Shockley-Ramo theorem [11, 12]. It gets more involved in multi-electrode detectors [13] and in crosstalk analysis. Signal processing with time-invariant systems has been extensively covered in the literature and is well understood.

Most innovations in signal processing in recent years have been in circuit implementations using monolithic CMOS technology. This technology has brought about a significant shift in the circuit concepts to time variant circuits due to the use of switched capacitance circuits for which CMOS transistors are well suited.

The noise analysis of time variant circuits brings up the question of whether to perform the analysis in frequency domain or in time domain. Analysis in frequency domain provides sufficient insight into time invariant circuits and it has been used in most of the literature. Frequency domain is less well suited for time variant circuit analysis as it does not provide much insight into the system transfer function. This is where the concept of the weighting function and Campbell's theorem [14] provide the tools which are simpler to use and provide more insight. While both analytical methods provide the same results in noise calculations, we note that particle detector signals are best described and are observed in the time domain, and so is the system response and the weighting function. In contrast, the noise analysis of narrow band circuits is best done in the frequency domain. The time domain analysis is based on the representation of noise as a random sequence of elementary impulses. In spite of our thinking and observing in the time domain, the device and circuit noise sources are customarily characterized in the frequency domain, e.g., we talk about the "white noise", "1/f noise", etc. Thus we switch our thinking between the two (Fourier transform related) domains depending on which one provides better insight and is easier to analyze in a particular case.

This chapter is intended to provide some insight into detector signal processing. Detailed circuit design, particularly of the monolithic circuits, has been rapidly developing and there has been a proliferation of publications. Advanced simulation tools are being used for noise analysis. Sometimes such an analysis provides numerical results without providing much insight into the role of various noise sources and into the overall weighting function of the signal processing chain. We concentrate here on the interpretation of the weighting function and on those aspects of signal processing and noise that have been less covered in the literature such as the induced signals in multi-electrode (strip and pixel) detectors, the "*kTC*" noise, correlated sampling and basic properties of low noise charge amplifiers. Induced

signals are determined using the "weighting field" concept, and noise analysis is based on the "weighting function" concept. The former is based on electrostatics and the latter on superposition of noise impulse contributions to the variable (current, charge) measured by the readout system.

10.2 Charge Collection and Signal Formation in Detectors

10.2.1 Current Induced by the Moving Charge and the Weighting Field Concept

Figure 10.1 illustrates the Shockley-Ramo theorem for induced signals, current and charge. $\boldsymbol{E_w}$ is the weighting field in units of 1/cm, and it is a measure of electrostatic coupling between the moving charge and the sensing electrode. The procedure to calculate the induced current as a function of time is as follows. First, the weighting field is determined by solving Poisson's equation analytically or numerically assuming unity potential on the sensing electrode of interest and zero potential on all other electrodes. Next, the velocity of the moving charge, $v = \mathrm{d}x/\mathrm{d}t$,

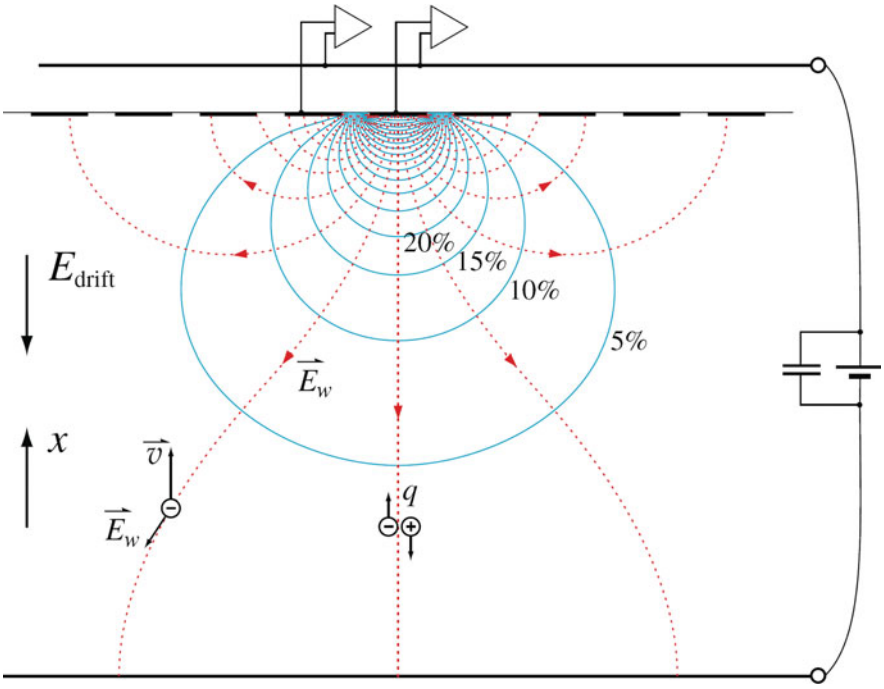

Fig. 10.1 Weighting potential (blue lines) and weighting field lines for planar strip electrode readout

as a function of position is determined from the operating (applied) field on the detector. This gives the induced current as a function of the position of the moving charge,

$$i = -q\,\vec{E}\cdot\vec{v}\,. \tag{10.1}$$

Third, the position of the moving *charge* as a function of time is determined by solving the equations of motion. This is necessary in the case of ballistic motion of charge, but it is simple in the case of transport by drift as the charge carriers follow the applied electric field. If we are interested only in the total induced charge and not in the waveforms, the induced charge is simply given by the difference in the weighting potentials between any two positions of the moving charge,

$$\begin{aligned} Q_s &= \int i\,dt = +\int \vec{E}_w\,d\vec{x}\,, \\ Q_s\,(1,2) &= q\,(V_{w2} - V_{w1})\,. \end{aligned} \tag{10.2}$$

An example of the weighting-field (potential) profiles is illustrated by the plot of equipotential lines for planar geometry with a strip sensing electrode. The operating (applied field) in this case is uniform and perpendicular to the electrodes. The weighting field map is in general quite different from that of the operating field; the two field maps are identical only in some special cases. The minus sign in Ramo's equation (Eq. 10.1) for the induced current results from the arbitrary assumption of induced current *into* the electrode being positive.

The sketch in Fig. 10.2a shows conceptually how the weighting field (potential) is defined: the sensing electrode is connected to unity potential, and all other electrodes to zero potential. The equipotential lines in Fig. 10.2b illustrate the solution for this case, showing two strips next to the sensing electrode. A great variety of results for the induced current and charge may arise in an electrode structure, such as this, depending on the particle type detected (distribution of ionization) and on the ratio of the charge observation measurement (or integration) time and the charge carrier transit time. The current waveforms shown are drawn qualitatively for a simple example. The operating field is assumed uniform and perpendicular to the electrode planes. Charge q_m traversing the full distance between the electrodes along line 1 is observed as $Q_1 = -q_m$, while the current decreases with distance from the sensing electrode 1, as the electrostatic coupling decreases. For a charge moving along line 2, the induced charge (i.e., the difference between the weighting potentials) is zero, if the measurement time is longer than the transit time. For a short measurement time a net induced charge is observed. The induced current waveform (the "crosstalk signal") is bipolar, since the weighting field direction changes along the path.

Figure 10.3 illustrates a simple case where the real (operating) electric field and the weighting field have the same form $= 1/d$. The induced current waveforms shown are for a semiconductor detector with different electron and hole mobilities. For extended ionization the waveforms result from superposition of the waveforms for localized ionization, and the currents decrease as the carriers arrive at the electrodes from different initial positions within the bulk of the detector.

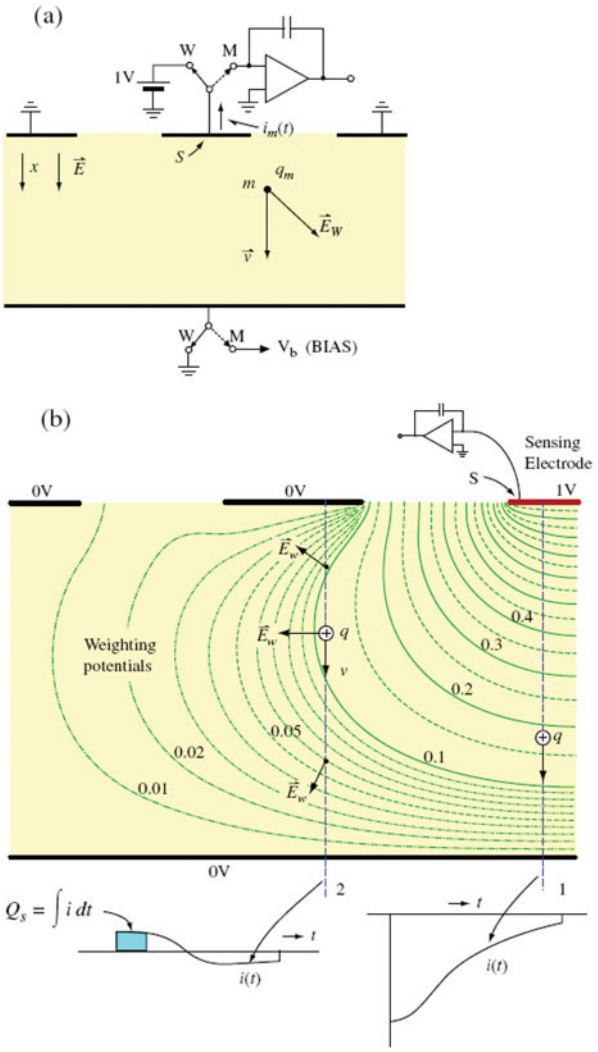

Fig. 10.2 Definition of the weighting potential: Solution of the Laplace equation for unity potential at the sensing electrode and zero potential at all other electrodes. From Radeka [9] Annual Reviews, www.annualreviews.org, by permission

10.2.2 Induced Current and Charge in Strip and Pixel Electrodes: Shielding Effect

The shielding effect is proportional to the ratio of the distance between the planar electrodes and the strip width (i.e., pixel radius). The shielding effect is more pronounced for pixels than for strips. The result of these configurations is that the

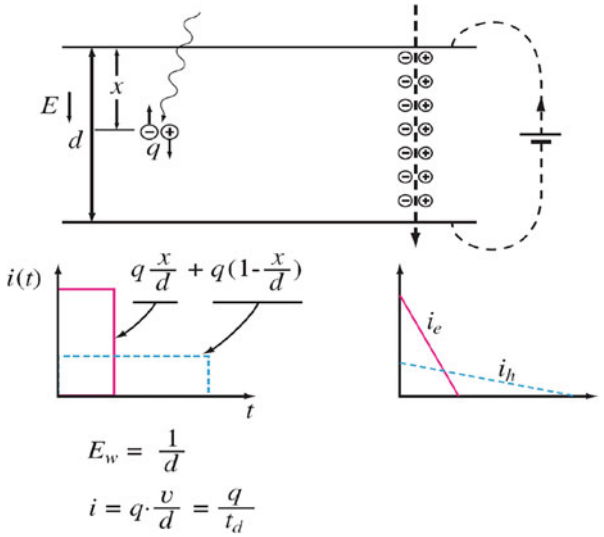

Fig. 10.3 Induced currents in infinite planar electrodes for localized and extended ionization

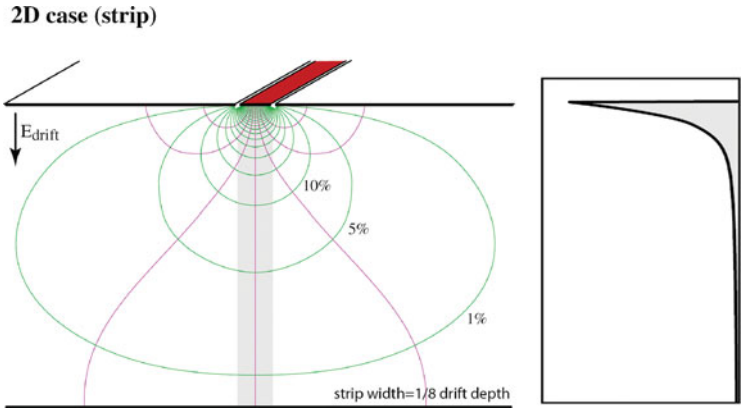

Fig. 10.4 Weighting field (potential) for strip electrode configuration

signal charge (integral of the induced current) is independent of the position of the origin of ionization for most of the volume of the detector except near the readout electrodes. This effect is used in detectors where only electrons are collected during the integration time, such as Cadmium Zinc Telluride (CZT), and some gas and noble liquid detectors. To illustrate this, histograms are shown in Figs. 10.4 and 10.5 for a strip and pixel illuminated by a beam of penetrating x-rays absorbed uniformly through the detector.

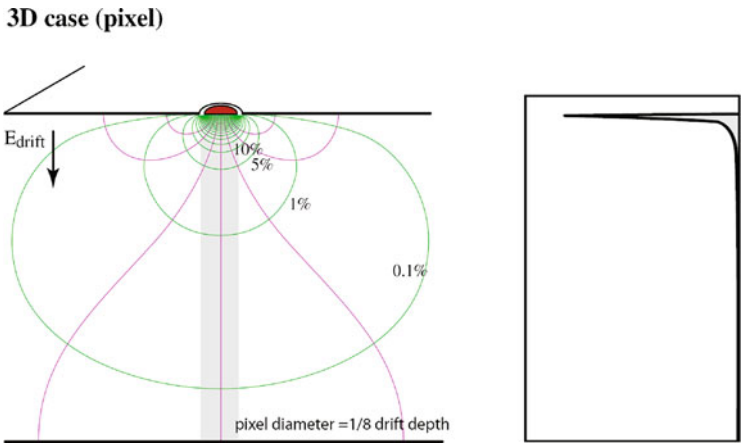

Fig. 10.5 Weighting field (potential) for pixel electrode configuration

10.2.3 Weighting Potential and Induced Charge in Co-Planar Electrodes

Coplanar grid readout was introduced for unipolar charge sensing by Luke [15] and it is commonly used with Cadmium Zinc Telluride (CZT) detectors. In such materials only electrons are collected (from the ionization produced by gamma rays or x-rays), the holes suffering from very low mobility and trapping. With parallel plane electrodes the induced charge for single carrier collection is dependent on the position (depth) where the ionization took place. In the coplanar grid concept one set of alternate strips is biased slightly more positively with respect to the other set of strips. This results in a drift field such that the signal electrons are collected on one set of strips only, Fig. 10.6. The weighting potential (field) for both sets of strips is identical, Fig. 10.7. The induced charges and currents are quite different, Figs. 10.8 and 10.9. Their respective differences are independent of the position, as can be concluded by following the weighting potential plot from any point on the planar sloped part of the plot to unity weighting potential for the collecting electrode, and (across the saddle) to zero potential for the non-collecting electrode, Fig. 10.9.

10.3 Noise: Origin and Properties

10.3.1 Noise Process and Noise Variance

The basis of a noise process can be represented as a sequence of randomly generated elementary impulses that has a Poisson distribution in time and mean rate of occurrence $\langle n \rangle$. Upon acting on a physical system with impulse response much

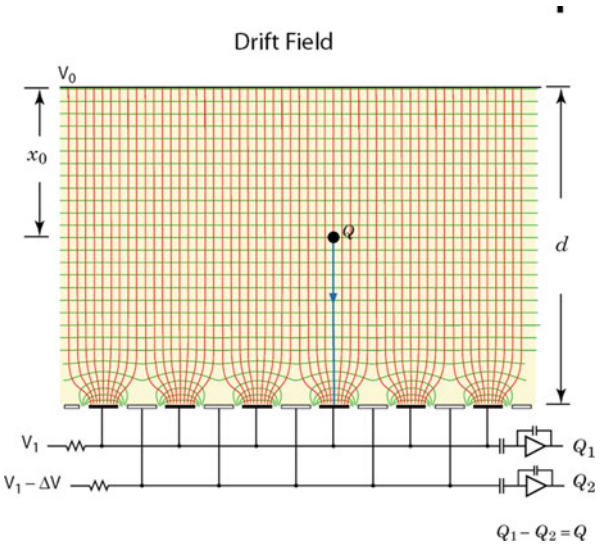

Fig. 10.6 Drift field for coplanar electrodes

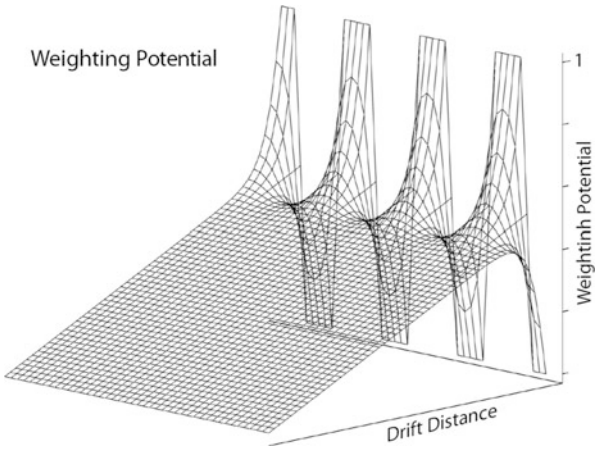

Fig. 10.7 Weighting potential for coplanar electrodes

longer than $\langle n \rangle^{-1}$, the characteristic noise waveforms (e.g., such as those we observe on an oscilloscope) are produced as a superposition of responses to individual impulses. The noise variance at the output of the physical system (a simple RC filter or a complete readout system) is calculated by using Campbell's theorem [14], which states that the sum of mean square contributions of all preceding impulses equals the variance. The expressions for the variance are given after subtracting the mean value. The variance is determined by the rate of impulses $\langle n \rangle$, their area q

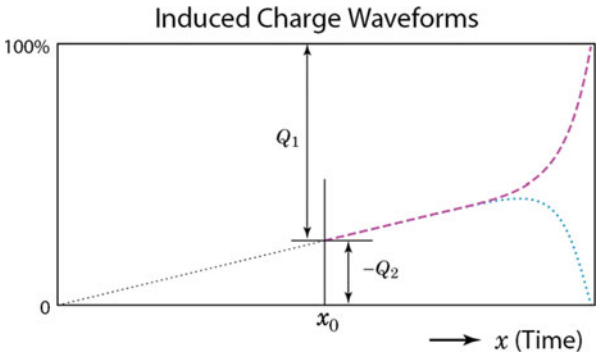

Fig. 10.8 Induced charges in coplanar electrodes: $Q_1 - Q_2 = const$ independently of x_0

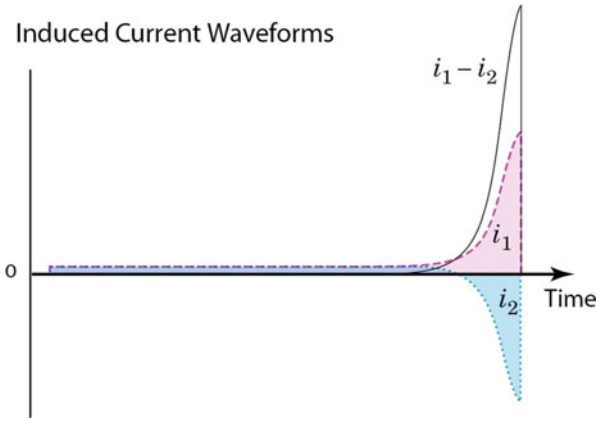

Fig. 10.9 Induced currents in coplanar electrodes

(charge), and by the impulse response $h(t)$, i.e., the weighting function $w(t)$ of the measurement system, the preamplifier and the subsequent readout chain,

$$\sigma^2 = \langle n \rangle \, q^2 \int_{-\infty}^{\infty} h^2(t)dt = \langle n \rangle \, q^2 \int_{-\infty}^{\infty} w^2(t)dt \; . \tag{10.3}$$

The noise variance is determined by the noise process, the rate of impulses $\langle n \rangle$, and their area q (charge), and by the impulse response $h(t)$. If we measure the variance and the $h(t)$, we can determine $\langle n \rangle q^2$, but we cannot determine $\langle n \rangle$ and q. Only when randomly generated carriers move in one direction, which results in a mean current $I_0 = \langle n \rangle q$, can the rate and the charge of impulses be determined from $\sigma^2$and I_0. It is shown in Ref. [9] that $\langle n \rangle q^2$ equals the mathematical (two-sided) noise current spectral density, whereas $\overline{i_n^2} = 2 \langle n \rangle \, q^2$equals the physical (single-sided) one, to be used in calculations of the equivalent noise charge (ENC) in Sect. 10.4.2.

10.3.2 A Model for Generation of Noise Spectra

Almost any noise spectrum can be generated from a random sequence of impulses (i.e., white noise with "infinite bandwidth") by using an appropriate filter, as illustrated in Fig. 10.10. These impulses may be either of only one polarity or of both polarities (current thermally generated in a p-n junction under reverse bias in the former, and with zero bias in the latter case). The mean value depends on the impulse polarities, but the variance does not.

"Infinite bandwidth" implies a noise spectrum which is flat over the frequency range where our measurement system has a non-zero response. Simple integration of white noise results in "random walk" with $1/f^{2}$ spectrum. An elementary impulse response for generation of this noise is the step function $U(t)$. Generation of $1/|f|$ noise is somewhat more elaborate. It requires fractional integration of *order one half*. The impulse response of the transforming filter is $U(t)/t^{1/2}$, as shown in the figure. The basic feature of any noise generating mechanism for low frequency divergent noises is an "infinitely long memory", i.e., very long memory, for individual independent elementary perturbations.

For a discussion of the basics of power-law spectra and of fractional integration see Ref. [16].

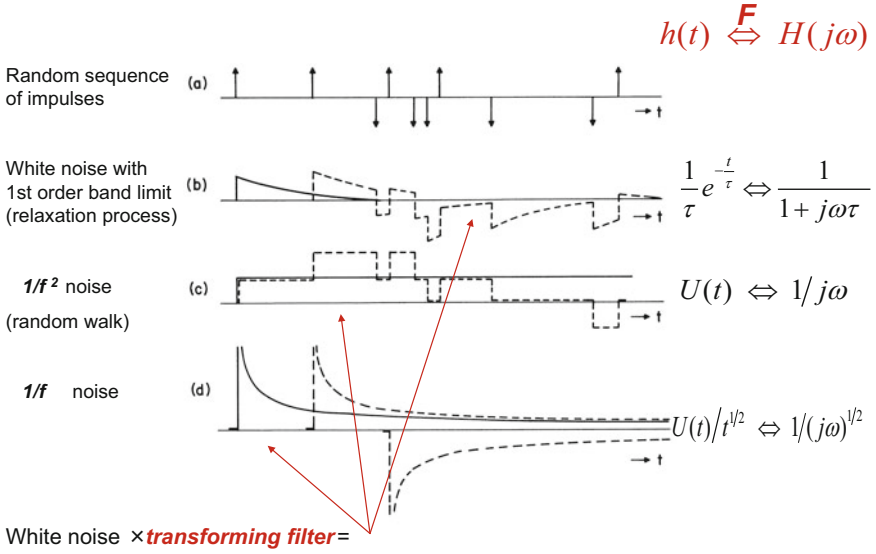

Fig. 10.10 Generation of some basic noise spectra from white noise by a transforming filter

10.3.3 Random Telegraph Noise and 1/f Noise

A noise spectrum very close to $1/|f|$ can be generated by superposition of relaxation processes with uniform distribution of life times, as illustrated in Fig. 10.11 The relaxation process is described by $U(t)\exp(-t/\tau)$, which represents a step change with exponential decay. Trapping-detrapping in semiconductors is one such possible mechanism for generation of $1/|f|$ noise. Since a simple RC integrator has the same response, a hardware filter which transforms white noise into $1/|f|$ noise can be made requiring about one time constant (one RC circuit) per decade of frequency, as shown in Ref. [16].

A single trap in a very small (minimum size) MOS transistor results in a drain current modulation known as random telegraph noise (RTS). This noise presents a limit to sensitivity in imaging arrays with a pixel capacitance of a few femtofarads and other noise sources reduced to a few electrons rms. There is extensive literature on RTS, e.g., Refs. [17–20].

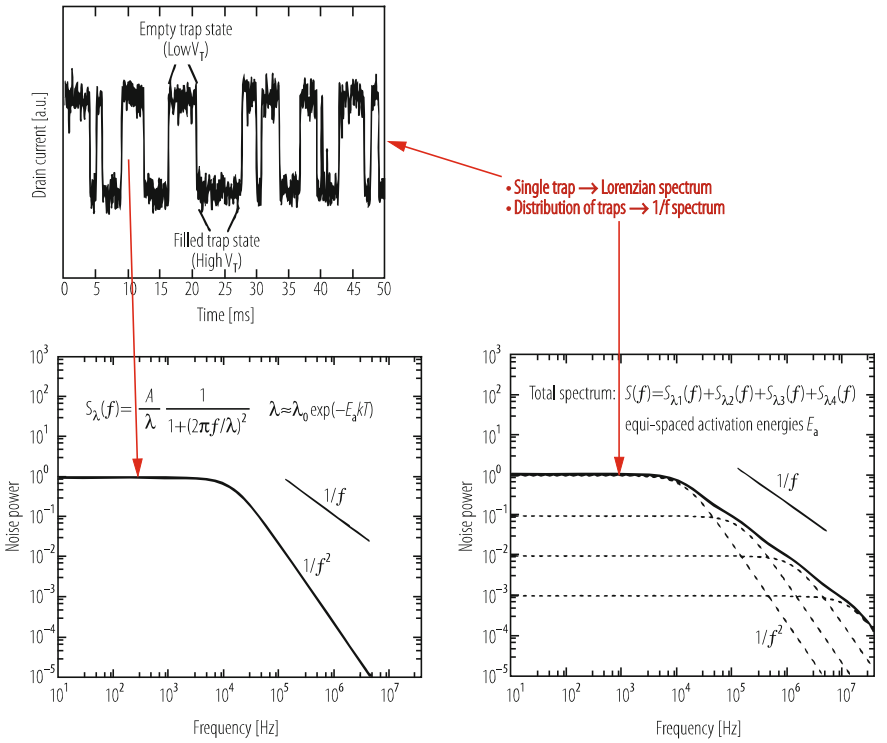

Fig. 10.11 Generation of random telegraph noise (left) and of 1/f noise (right) by trapping-detrapping. Adapted from Compagnoni et al. [17]

$1/|f|$ noise is one of the fractal processes, and its waveform preserves the same features independently of the time scale [16]. Another expression of this is independence of the measurement variance on the time scale of the measurement as long as the ratio of the high frequency and the low frequency cutoffs remains constant. As the bandpass moves along the frequency spectrum the spectral density integral (i.e., the measurement variance),

$$\sigma^2 \propto \int_{f_l}^{f_h} \frac{df}{f} = \ln\left(\frac{f_h}{f_l}\right) \tag{10.4}$$

remains constant for $f_h/f_l = const.$ In detector pulse processing it is well known that the contribution of $1/|f|$ noise to the equivalent noise charge (ENC) remains independent of the shaping time, as will be shown in the following Sect. 10.4.2. Physical mechanisms of $1/f$ noise are discussed in Ref. [21].

10.4 Noise in Charge Measurements

10.4.1 Sources of Noise in Charge Amplifiers

Principal noise sources in charge amplifiers and an equivalent diagram for calculation of the equivalent noise charge (ENC) are shown in Fig. 10.12.

Two elementary noise generators are included in the equivalent circuit, a series noise voltage generator representing the noise in the amplifying device, and a parallel noise current generator representing various noise sources not inherent to

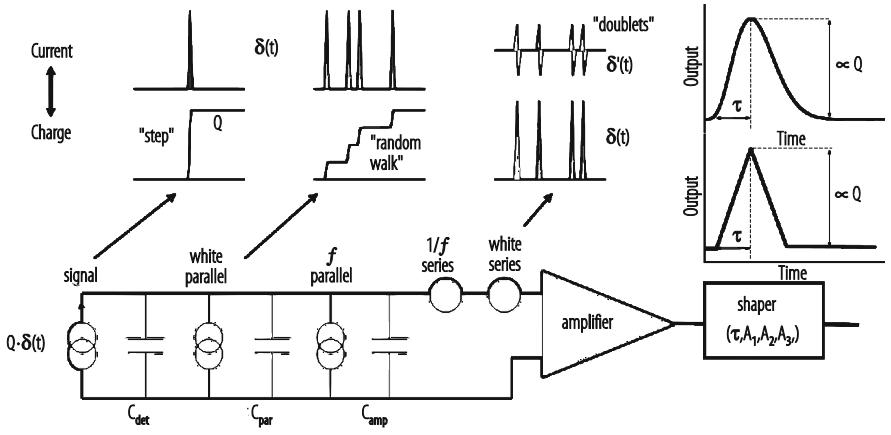

Fig. 10.12 An illustration of noise sources in charge amplifiers, as a Poisson sequence of elementary *current* pulses into the input capacitance, or *voltage* pulses on the capacitance

amplification (detector leakage current noise, parallel resistor noise, etc.). Both types of noise are assumed to have a white spectrum. Two forms of presentation in terms of a sequence of random pulses are shown, as charge (or voltage) at the input of the amplifier, and as a current injected into the input capacitance (comprised of the detector + amplifier parasitic capacitances). The presentation of the series noise in terms of a current into the detector input is the derivative of the charge (voltage) representation. The sequence of voltage impulses representing the amplifier series noise thus corresponds to an equivalent sequence of current doublets (derivatives of delta function) injected at the detector. The parallel noise is by its origin a current source in parallel with the detector, and it is presented by a sequence of impulses (delta functions). *It is this difference in the location of the two white noise sources with respect to the detector capacitance that makes their apparent noise spectra and their effect on the measurement quite different.* ENC due to the former is inversely proportional to the square root of the peaking time, and proportional to it due to the latter. The series $1/|f|$ noise contribution to ENC is independent of the peaking time, as indicated in Fig. 10.14. The $1/|f|$ noise due to a dissipative dielectric depends on the dielectric loss factor $\tan(\delta)$, as will be discussed in Sect. 10.4.7. It can be significant with detector-amplifier connections on glass fibre circuit boards.

10.4.2 Equivalent Noise Charge (ENC) Calculations

Calculation of equivalent noise charge (ENC) for a signal processing chain described by a weighting function $w(t)$ is summarized in the following.

The noise calculation is performed in the time domain by using Campbell's theorem Eq. (10.3), that is by superposition of effects of all random *current* impulses illustrated in Fig. 10.12. The weighting function is normalized to unity so that the definition of *ENC is the noise charge which produces an output of the same magnitude as an impulse signal of equal charge*. For calculation of ENC due to the series *voltage* noise, we will use the representation in terms of an equivalent current generator connected in parallel with the detector. This requires differentiation of the sequence of voltage impulses. Each resulting doublet $C_{in}\delta'(t)$ acting upon the weighting function $w(t)$ produces by convolution $C_{in}w'(t)$. The equivalent noise charge (ENC) is then given by,

$$ENC^2 = \frac{1}{2}e_n^2 C_{in}^2 I_1 + \pi C_{in}^2 A_f I_2 + \frac{1}{2}i_n^2 I_3, \tag{10.5}$$

where $\overline{e_n^2} = 4kTR_s$ is the physical (single-sided) noise *voltage* spectral density for series noise in V^2/Hz expressed in terms of an equivalent series noise resistance. The second term is due to the series $1/f$ noise. The $1/f$ noise physical spectral density is defined as A_f/f in [V^2/Hz]. The third term is due to the parallel noise, where $i_n^2 = 2qI_0 = 4kT/R_p$ is the physical noise *current* spectral density due to either a current or a resistance in parallel with the detector.

I_1, I_2, I_3 are the noise integrals for the *series* (*voltage*) white noise and the *1/f noise*, and for the *parallel* (*current*) noise, respectively. The integrals are derived in the time domain from Campbell's theorem Eq. (10.3) and expressed in the frequency domain using Parseval's theorem [9],

$$I_1 = \int_{-\infty}^{\infty} \left[w'(t)\right]^2 dt = \frac{1}{2\pi} \int_{-\infty}^{\infty} |H(j\omega)|^2 \omega^2 d\omega = \frac{A_1}{\tau}, \tag{10.6}$$

$$I_2 = \int_{-\infty}^{\infty} \left[w^{(1/2)}(t)\right]^2 dt = \frac{1}{2\pi} \int_{-\infty}^{\infty} |H(j\omega)|^2 \omega d\omega = A_2, \tag{10.7}$$

$$I_3 = \int_{-\infty}^{\infty} [w(t)]^2 dt = \frac{1}{2\pi} \int_{-\infty}^{\infty} |H(j\omega)|^2 d\omega = A_3 \tau, \tag{10.8}$$

where τ is the time width parameter of the weighting function, either the peaking time of the function, or some characteristic time constant of the filter implemented in hardware (or software in case of digital filtering).

Noise contributions for both types of white noise due to various segments (piece-wise linear approximation) of the weighting function are shown in Fig. 10.13 (expressions for integrals I_1 and I_3). In these calculations, either the *impulse response* $h(t)$ of the system or the *weighting function* $w(t)$ (the mirror image of the impulse response) can be used for time-invariant systems. For time-variant (gated or switched) systems, only a weighting function describes the performance correctly, while an apparent impulse response (waveform at the output) is not correct and can be misleading. Steepest parts of the weighting function contribute most to ENC_s, as they correspond to larger bandwidth. Flat parts do not contribute anything. In contrast, ENC_p is largely proportional to the width of the weighting function where it has any significant value.

A bipolar weighting function, i.e., impulse response h(k), as shown in Fig. 10.13, with equal lobes would result in square root of two higher ENC than for a unipolar function (single lobe). If the amplitude of the second lobe is less than one half, its rms noise contribution becomes small (<12%).

The half-order integral I_2 for 1/*f* noise is not amenable to such a simple interpretation, and it will be discussed in Sect. 10.4.6.

Equations (10.6, 10.7, and 10.8) provide an insight into the general behaviour of signal processing systems with respect to noise. The ENC due to the series white amplifier noise is proportional to the slope (~1/t) of the weighting function and therefore proportional to the bandwidth of the system. The ENC due to parallel white noise is proportional to the width of the weighting function and therefore to the overall integration time. If the weighting function form remains constant the ENC due to *1/f* noise is independent of the width of the weighting function, since the ratio of the high frequency cutoff and low frequency cutoff remains constant,

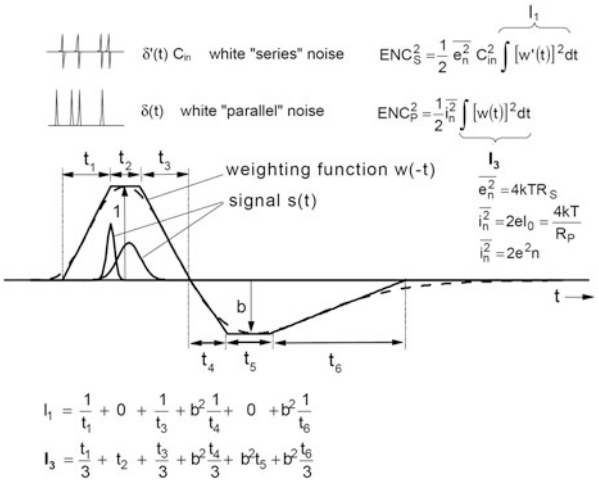

Fig. 10.13 An illustration of noise contributions for both locations of white noise sources (series and parallel) due to various segments of the weighting function. Such a piece-wise linear approximation of the weighting function provides an estimate of the noise within a few percent of accurately computed integrals I_1 *and* I_2

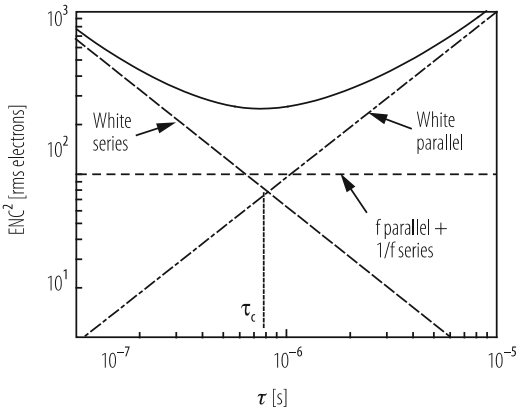

Fig. 10.14 An example of general behaviour of equivalent noise charge (ENC) as a function of the width parameter τ of the weighting function. 1/*f* noise raises the noise minimum but does not affect its position on the time scale

Eq. (10.4). This is illustrated in Fig. 10.14. From Eqs. (10.5, 10.6, and 10.8) the optimum width parameter of the weighting function is given by,

$$\tau_{opt} = \left(R_s R_p\right)^{1/2} C_{in} \left(A_1 \Big/ A_3\right)^{1/2}, \tag{10.9}$$

and it is not affected by 1/*f* noise.

10.4.3 Weighting Function

The concept of weighting function is very useful for time domain noise analysis of time variant, sampled and switched systems. The role of "pulse shaping," "signal filtering," or "signal processing" is to minimize the measurement error with respect to the noise, various baseline offsets and fluctuations, and at high counting rates to minimize the effects of pulse overlap or pileup. The term "pulse shaping" implies that the amplifier-filter system is time invariant. In such a system the system parameters do not vary during the measurement and a single measurement of amplitude or time is performed. Such a system is described completely by its impulse response.

In signal filtering, we also use time-variant methods, such as capacitor switching and correlated multiple sampling of the signal. The filtering properties of a time-variant system are described by its weighting function $w(t)$. *The weighting function describes the contribution that a noise impulse, occurring at time t_i, makes at the measurement t_m*, as illustrated in Fig. 10.15. It is essentially a measure of the memory of noise impulses (or any other signals) occurring before the observation time t_m. As shown, *the weighting function for time-invariant systems is simply a mirror image in time of the impulse response, with its origin displaced to t_m*. For a time-variant system, the impulse response (output waveform) is generally quite different from its weighting function. In some cases time-invariant and time-variant processing could be devised to produce the same result, i.e., both methods will be described by the same weighting function, while their implementation will be quite different. The noise-filtering properties of any weighting function for detector signal processing can be most easily determined by the time domain analysis technique shown in Fig. 10.13. The time domain analysis method based on Campbell's theorem was first introduced by Wilson [22], and subsequently elaborated in Refs. [9, 23, 24].

A composite weighting function for multiple correlated sampling is obtained by superposition of weighting functions for individual samples. This is illustrated

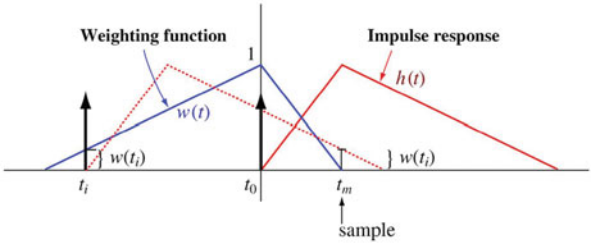

Fig. 10.15 An illustration of the weighting function $w(t)$ corresponding to impulse response $h(t)$. A unit noise impulse at t_i contributes $w(t_i)$ at the time t_m of the peak of response to the signal impulse at t_0. The weighting function in this case of a simple time-invariant filter is a mirror image of the impulse response delayed by the sample (i. e., measurement) time t_m

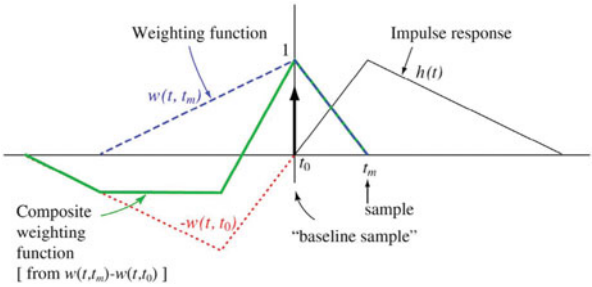

Fig. 10.16 Composite weighting function for *correlated double sampling* (CDS). Time-invariant filtering ("pulse shaping") described by an impulse response $h(t)$ is assumed prior to sampling

for *correlated double sampling* (*CDS*), a technique commonly used for readout of CCD's and large pixel arrays, Fig. 10.16. Single sample processing is described by a symmetrical triangular impulse response approximating single RC differentiation and one or two RC integrations. The single sample weighting function with respect to the sampling time at t_m is shown (dashed), and it is a mirror image of the impulse response. It is assumed that a (delta function) signal of interest will arrive at time t_{0+}, and produce a response described by the impulse response. In double correlated sampling another sample is taken at t_0, just before the arrival of the signal. This sample, sometimes called "baseline sample", is subtracted from the "signal or measurement sample". The weighting function for the baseline sample is shown inverted and earlier in time by t_m-t_0.

The composite weighting function (thicker solid line) is bipolar and it has area balance. This is another way of saying that CDS has zero dc response and that it attenuates (but does not eliminate) baseline fluctuations at low frequencies. The ENC can be easily calculated from such a composite weighting function using the technique for time domain noise analysis shown in Fig. 10.13. A noise analysis of such a case in the frequency domain and without the use of a composite weighting function is considerably more time consuming.

10.4.4 Simple ENC Calculation for Series White Noise

Following on the discussion in Sect. 10.4.2 and referring to Fig. 10.17, a simple relation for the equivalent noise charge (ENC_s) due to *series white noise* follows,

$$ENC_s^2 = (1/2)\, e_n^2 C_{in}^2 I_1, \tag{10.10}$$

where

$$I_1 = \int_{-\infty}^{\infty} \left[w'(t)\right]^2 dt = {}^{2}\Big/_{t_m} = {}^{A_1}\Big/_{t_m}, \tag{10.11}$$

$$ENC_s = {}^{e_n C_{in}}\Big/_{t_m^{1/2}}. \tag{10.12}$$

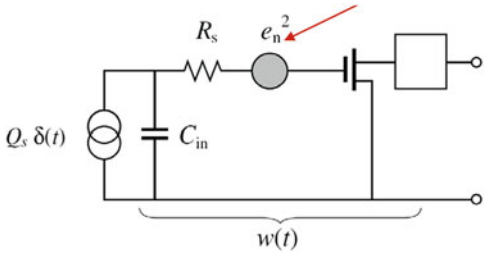

Fig. 10.17 Simplified equivalent circuit for calculation of equivalent noise charge (ENC) due to amplifier series white noise

It requires the knowledge of three parameters: noise spectral density e_n, total input capacitance (detector + amplifier) C_{in}, and peaking time t_m of the triangle approximating the weighting function. Such an approximation is useful for noise estimation, since the series noise coefficient for a fifth order semi-Gaussian weighting function with equal peaking time, $A_1 = 2.2$, differs by only ~10% from $A_1 = 2$ for the triangular function. In a preamplifier design, the expected e_n can be determined from the operating conditions (current and transconductance) of the first transistor, or from a more complete equivalent circuit of the input transistor shown in Sect. 10.5.2. *A primary objective of low noise amplifier design is to make the noise contributions of all other circuit components negligible compared to the input transistor.* Eq. (10.12) describes simply also the noise charge slope with respect to detector capacitance (in pF),

$$\partial\left(ENC_s/q_e\right)/\partial C = e_n/t_m^{1/2}\ \left[\text{rms electrons/pf}\right] \tag{10.13}$$

10.4.5 Simple ENC Calculation for Parallel White Noise

From Sect. 10.4.2 and Figs. 10.13 and 10.18 simple relations follow for ENC_p due to parallel shot noise and resistor (thermal) noise. The gated integrator case, where the weighting function equals unity for the duration of the gate, illustrates that the ENC_p for shot noise is simply the square root of the variance of a Poisson sequence of impulses counted for a time t_G .

$$ENC_p = (q_e I_0 t_G)^{1/2} = \left(q_e^2 n t_G\right)^{1/2} = q_e (n t_G)^{1/2} = q_e n_G^{1/2}. \tag{10.14}$$

By Campbell's theorem the contribution of each impulse to the variance is determined by the weighting function, and for a given weighting function the parallel noise integral I_3 has to be determined. For an approximation by a triangle with a peaking time t_m, $I_3 = (2/3)t_m$. The parallel noise contribution for the triangular weighting function is the same as for gated integration one third as wide.

The contribution by the parallel resistor thermal noise can be compared simply to the shot noise by the "*50 mV rule*": a dc current I_0 causing a voltage difference of

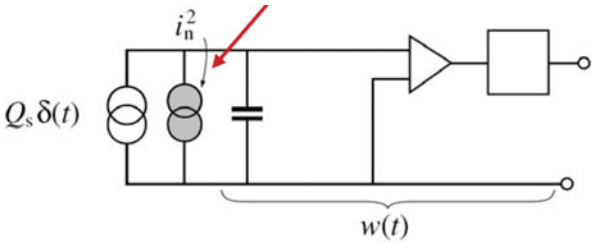

Fig. 10.18 Simplified equivalent circuit for calculation of equivalent noise charge (ENC) due to detector and amplifier parallel white noise (bias or feedback resistance, detector leakage current, tunneling gate current in MOS, base current bipolar junction transistor)

~50 mV on a resistor R_p contributes a shot noise equal to the thermal noise of that resistor at room temperature; from $4kT/R_p = 2q_e\ I_0$: $R_p\ I_0 = 2kT/q_e$.

10.4.6 Calculation and Estimation of ENC for 1/f Noise

1/*f* noise becomes a limiting factor in many physical measurements. We can imagine reducing the series white noise in charge measurements to a very low level by continuing to increase the measurement (integration) time τ, provided the parallel (leakage or dark current) noise is very low. We would eventually reach the "noise floor" due to the 1/*f* noise. Once the 1/*f* noise spectral density is determined experimentally and defined by the parameter A_f in [V^2] as in Eq. (10.5), ENC can be calculated by the integral I_2, Eq. (10.7). In the time domain this is an integral of a fractional-order (half-order) derivative squared of the weighting function (a mathematical operation which cannot be called "trivial" before one learns how to do it, and it can be considered "tedious" at best). In the frequency domain the calculation is somewhat easier for time-invariant systems, but for time-variant systems defining the transfer function $H(j\omega)$ is more difficult and less intuitive than determining the weighting function.

We illustrate this here on the example of a commonly used weighting function of trapezoidal form as shown in Fig. 10.19. There are many different hardware implementations of this function in different applications. Time-invariant versions have used delay line clipping and higher order RC prefilters. Gated integrator and higher order prefilters have been used in several applications, starting with germanium gamma-ray detectors [25]. This function is widely used with CCDs in astronomy, implemented by correlated double sampling and dual-ramp integration.

We define the trapezoidal weighting function by the width of the ramp τ_p and the flat top as a fraction of the ramp, $\Delta\tau_p$. The equivalent noise charge for 1/*f* noise is then,

$$ENC_f^2 = \pi C_{in}^2 A_f A_2, \tag{10.15}$$

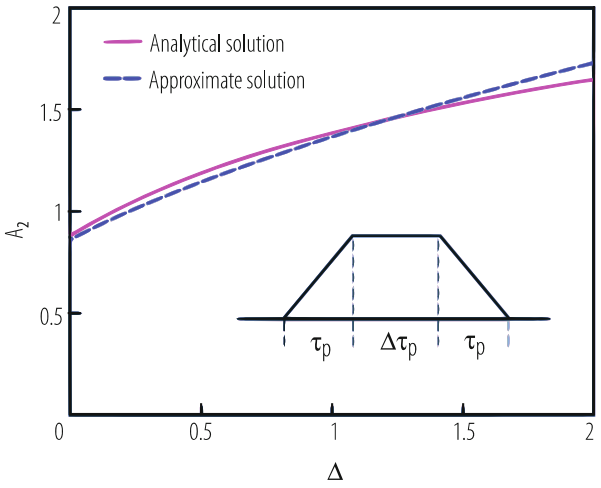

Fig. 10.19 1/*f* noise coefficient A_2, Eq. (10.7), for trapezoidal weighting function. *Solid line*: analytical solution, Eq. (10.18); *dashed*: approximate solution, Eq. (10.22)

where

$$A_2 = \int_{-\infty}^{\infty} \left[w^{(1/2)}(t) \right]^2 dt. \tag{10.16}$$

The half order derivative of the weighting function, $w^{(1/2)}(t)$, is obtained by convolution of $w'(t)$ with the elementary pulse $U(t)/t^{1/2}$ for 1/*f* noise shown in Fig. 10.10d,

$$w^{(1/2)}(t) = \left(1/\sqrt{\pi t} \right) * w'(t), \text{ for } t \geq 0+ \tag{10.17}$$

Using *Mathematica,* and after some manipulation, the result for A_2 is, [26],

$$A_2 = \frac{1}{\pi} \left[\Delta^2 \ln \Delta + (2+\Delta)^2 \ln (2+\Delta) - 2(1+\Delta)^2 \ln (1+\Delta) \right]. \tag{10.18}$$

The coefficient A_2 vs the flat top Δ of the trapezoidal weighting function is plotted in Fig. 10.19.

The effect of the series 1/*f* noise is lowest for a triangular weighting function, $\Delta = 0$, which is also the case for the series white noise, Eqs. (10.10, 10.11, and 10.12). As the flat top is made longer, A_2 increases, since such a trapezoidal function has a higher ratio of its cutoff frequencies, which results in integrating a wider band of the *1/f* noise spectrum, Eq. (10.4).

An almost identical result for A_2 has been obtained by a calculation in the frequency domain and described in a study of CCD noise performance [27].

Since such exact calculations of ENC_f for any weighting function can be time consuming, we emphasize here a simple estimation method, which provides results sufficiently close to the exact calculations for most purposes. It has been pointed out by Gatti et al. [28] that the three integrals in Eqs. (10.6, 10.7, and 10.8) have to satisfy the Cauchy-Schwartz inequality,

$$\int_{-\infty}^{\infty}\left[w^{(1/2)}(t)\right]^2 dt \le \left\{\int_{-\infty}^{\infty}\left[w'(t)\right]^2 dt \bullet \int_{-\infty}^{\infty}[w(t)]^2 dt\right\}, \tag{10.19}$$

that is,

$$A_2 \le (A_1 A_2)^{1/2}. \tag{10.20}$$

Thus there is an upper limit to A_2 in relation to A_1 and A_3 which are easily calculated from Fig. 10.13, or Eqs. (10.6, 10.7, and 10.8). A study of the most commonly used weighting functions, [28], reveals that $A_2/(A_1A_3)^{1/2}$ falls between 0.64 and 0.87, a spread of less than ±8% in the calculation of rms noise, so that for the estimation of 1/*f* noise the following approximate relation can be used,

$$A_2 \approx 0.75(A_1 A_3)^{1/2}. \tag{10.21}$$

For the trapezoidal weighting function in Fig. 10.19, $A_1 = 2$ and $A_3 = \Delta + 2/3$, and the approximation for this case is,

$$A_2 \approx 0.75\left[2\left(\Delta + {}^{2}\!/_{3}\right)\right]^{1/2}. \tag{10.22}$$

Figure 10.19 shows that this approximation is within a few percent of the exact analytical solution, Eq. (10.18).

In any noise analysis of charge amplifiers one will have already calculated, or otherwise determined the values of A_1 and A_3, so that the information about the filtering (pulse shaping) effect on the series and parallel white noise will readily also provide an estimate of the 1/*f* noise,

$$ENC_f^2 = \pi C_{in}^2 A_f A_2 \approx \pi C_{in}^2 A_f \left(0.75\sqrt{A_1 A_3}\right). \tag{10.23}$$

It is interesting to note that for a Gaussian weighting function $A_2 = 1.00$, for a triangular weighting function 0.88, for a fourth order semi-Gaussian 1.02, for CR-RC 1.18.

A_f is a parameter resulting from a measured spectral density and it does not contain any specific information about the properties of the amplifying device unless other parameters are known.

For input transistor optimization a parameter which is to the first order independent of the device dimensions is more useful [29], $K_f = A_f\ C_{gs}$ [J]. This constant

ranges from 10^{-27} J for junction field-effect transistors (JFETs) to ~10^{-25} J for p-channel and ~ 10^{-24} J for n-channel MOS transistors.

For an accurate calculation of the noise charge for noise spectra departing from the three-term power-law representation ("white series voltage noise", "1/*f* series voltage noise", and "white parallel current noise"), circuit simulation and numerical calculation are the tools of choice to obtain accurate results. The discussion here was intended to provide some insight: *ENC_f depends only on the shape of the weighting function but not on the time scale.*

10.4.7 Noise in Dielectrics

Thermal fluctuations in dielectrics generate a noise which is quantitatively related to the parameters describing dielectric losses. This type of noise and its importance for detectors was first studied in [30] and then summarized in [31]. For a dielectric with low losses, the dissipation factor or the loss factor D (equal to the imaginary part ε "of the permittivity $\varepsilon = \varepsilon' + j\varepsilon''$) is independent of frequency in the range of interest for particle and photon detectors (~10^4 to 10^8 Hz). It can be defined as $D = G(\omega)/(\omega C_{diel})$, where $G(\omega)$ and C_{diel} are the loss conductance and the capacitance of the dielectric as measured on an impedance bridge at an angular frequency ω. According to the fluctuation-dissipation theorem [32, 33], and using the Johnson-Nyquist formula for thermal noise, a dissipative dielectric generates a noise current with a spectral density,

$$i_n^2 = 4kT\,G\,(\omega) = 4kT\,D\omega C_{diel}. \tag{10.24}$$

The equivalent noise charge ENC_{diel} due to dielectric noise can be calculated using Eq. (10.7),

$$ENC_{diel}^2 = 2kT\,DC_{diel}A_2. \tag{10.25}$$

Following on the discussion in the previous section we assume here $A_2 = 1.2$,

$$ENC_{diel}^2 = 2.4kT\,DC_{diel}. \tag{10.26}$$

We note that the spectral density (Eq. 10.24) upon integration on the input capacitance becomes 1/*f*, and therefore the equivalent noise charge due to dielectric noise is independent of the width (the time scale) of the weighting function.

The noise from lossy dielectrics may pose in some detectors a lower limit to total noise. If a lossy dielectric contributes 1 pF, such as a glass fibre board with $D \approx 2{\cdot}10^{-2}$, this alone would present a lower limit of $ENC_{diel} \approx 86$ rms electrons. Best dielectrics (e.g. Teflon, polystyrene, quartz) have $D \approx 5{\cdot}10^{-5}$, which results in ~5 rms electrons. This noise contribution to the charge measurement can be reduced only by reducing C_{diel} (and/or the temperature).

10.5 Gain Mechanisms and Noise in Transistors

10.5.1 Gain Mechanism, Electron Transit Time, Unity-Gain Frequency

The charge control concept as the basis for the gain mechanism in all three-terminal amplifying devices (transistors) was discussed in Ref. [9]. The "control charge" Q_c is illustrated in Fig. 10.22.

The relation among the control capacitance C_{gs}, the transconductance g_m, the electron transit time τ_e and the unity gain frequency f_T is summarized by,

$$\begin{aligned} &\Delta Q_c/\Delta I_d = \tau_e = C_{gs}\Delta V_{gs}/\Delta I_d = C_{gs}/g_m \rightarrow C_{gs} = g_m\tau_e, \\ &f_T \approx {}^{1}\Big/_{(2\pi\,\tau_e)} = \left({}^{1}\Big/_{2\pi}\right)\left({}^{g_m}\Big/_{C_{gs}}\right). \end{aligned} \tag{10.27}$$

NMOS transistors in submicron range (channel length below ~0.25 microns) will have a unity gain frequency in the range 10 to 100 GHz when operated in strong inversion. These same devices will be operated in weak inversion to maximize the transconductance/current ratio and the power dissipation in detectors with large numbers of channels (pixels or strips). This means reduced transconductance with almost the same gate capacitance resulting in a unity gain frequency in the range of 1 GHz or less. This affects the speed of response and the stability considerations in the design of feedback amplifiers.

Equation (10.27) describe only a simplified basic relation among intrinsic device parameters. A very extensive treatment of charge control concepts for CMOS transistors including parasitic parameters and device operating conditions is given in Ref. [7].

10.5.2 Noise Sources in MOS Transistor

A brief overview of white noise sources in an NMOS transistor normalized to the intrinsic channel series noise resistance γ/g_{ms} is illustrated in Fig. 10.20 and Eq. (10.28) with γ typically in the range 0.5 to 1.0. The second term in Eq. (10.28) is the gate induced noise contribution [34]. The coefficient $\delta/5\gamma$ depends on the bias conditions. For estimation purposes $(\delta/5\gamma) \sim 1/3$. With capacitive sources, such as most radiation detectors, this term is usually negligible. In particular, at operating conditions to minimize the power in the input transistor, the optimum ratio C_{gs}/C_{in} is small. The contributions by the gate resistance and substrate resistance can be made

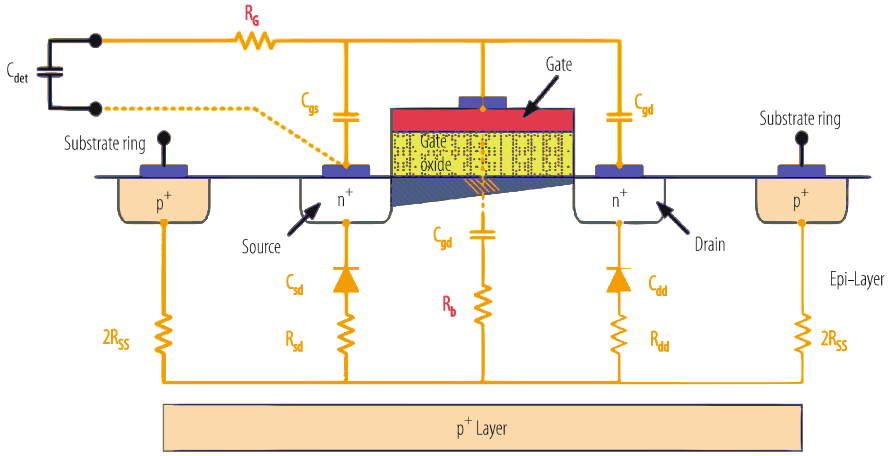

Fig. 10.20 An illustration of parasitic resistive noise sources in an NMOS transistor in addition to the channel noise γ/g_{ms}

small by the device design. The equivalent series noise resistance of the NMOS transistor can be summarized referring to the notation in Fig. 10.20 as,

$$\frac{R_{eq}}{\gamma/g_{ms}} = 1 + \frac{\delta}{5\gamma}\left(\frac{C_{gs}}{C_{in}}\right)^2 + \frac{1}{\gamma}\left(R_g g_{ms}\right) + \left(R_b g_{mb}\right)\frac{g_{mb}}{g_{ms}} + \frac{1}{\gamma}\left(R_b g_{ms}\right)\left(\frac{C_{gb}}{C_{in}}\right)^2. \tag{10.28}$$

10.5.3 Charge Transfer from Detector to Transistor: Capacitance Matching

In all cases where the amplifier is connected directly to the detector via a resistive conductor the charge produced by ionization is distributed among the detector capacitance, amplifier capacitance and any stray capacitance according to the ratio of capacitances, Fig. 10.21. Due to this, only a fraction of the charge of interest (the signal) arrives where it matters—that is to the conduction channel of the input transistor where it controls the drain (collector) current, as illustrated in Fig. 10.22. (An exception to this is if the two capacitors are connected by an inductor in which case the charge is transferred periodically between the two capacitors.) In case of a CCD the ionization charge is moved peristaltically in a potential well formed and driven by appropriate clock voltages applied to the gate electrodes. The charge shifted a few hundred (or thousand) times arrives at the collection electrode ("floating diode") which is connected to a source follower. In the CCD the charge arriving at the collection electrode is the original charge packet produced

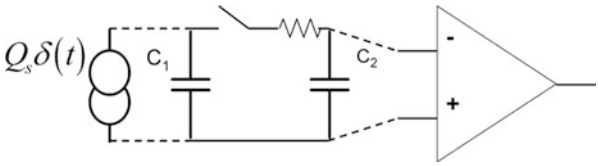

Fig. 10.21 Sharing of the induced ("collected") charge between the detector and amplifier capacitance

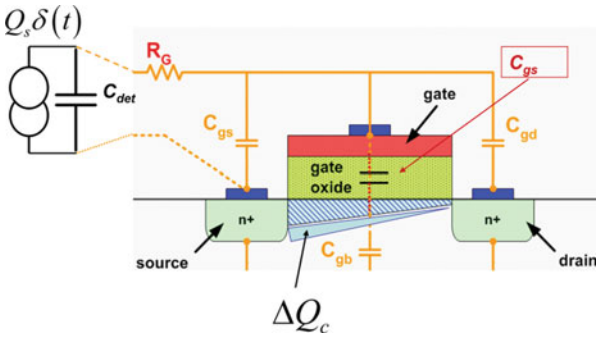

Fig. 10.22 An illustration of the *control charge* with respect to the *control capacitance* C_{gs}: $\Delta Q_c = Q_s/[1 + (C_{det} + C_{gsp} + C_{ds})/C_{gs}]$

by ionization except for a few electrons lost to trapping. The charge transport in a conductor is by a small displacement of a large number of free electrons. The CCD principle allows multiple measurements on the same charge packet as described in Ref. [35].

Optimization of the signal to noise ratio requires appropriate matching of the transistor active capacitance (which controls the current) to all other capacitances connected to the input—a subject addressed in some detail in Ref. [10].

The charge control concept expressed by Eq. (10.27) is at the basis of the gain mechanism in almost all electronic amplifying devices: it takes an increment of charge, ΔQ_c in Fig. 10.22, to cause a steady state change of the current in the conducting channel. From Eqs. (10.12 and 10.27) we can determine the lower limit for the charge sensitivity due to the series noise in terms of the electron transit time in the conducting channel. Scaling the device width (with no power limitation) to achieve the best signal-to-noise ratio requires that the control electrode capacitance equal (match) the detector capacitance, $C_{gs} = C_{det}$. With this and Eq. (10.27), the lowest noise for an electronic amplifier that could be achieved under ideal circumstances is given by,

$$ENC_{s\ opt} \cong 2\sqrt{2}\sqrt{kTC_{gs}}\sqrt{\tau_e / t_m}, \tag{10.29}$$

where t_m is the weighting function zero-to-peak time, as in Fig. 10.13, also referred to as the "integration time" or the "measurement time".

It is assumed here for simplicity that the equivalent series noise resistance is equal to the inverse of the device transconductance, i.e., $\gamma \sim 1$. While Eq. (10.29) is useful for estimation purposes and for establishing a lower limit for the amplifier series noise, the electron transit time is rarely used directly for noise calculations.

Accurate noise calculations usually rely upon the measured or known noise spectral density for a particular device and have to include parasitic capacitances and resistances, as indicated in Fig. 10.20.

10.6 Weighting Function Realizations: Time Invariant and Time Variant

10.6.1 Time-Invariant Signal Processing

A low order asymmetrical function (dashed), shown in Fig. 10.23, results in higher series noise (due to a steeper rise, see Fig. 10.13). A nearly symmetrical function requires a higher order signal processing chain, as shown.

A time-invariant circuit realization of a nearly symmetrical weighting function is described in Ref. [36].

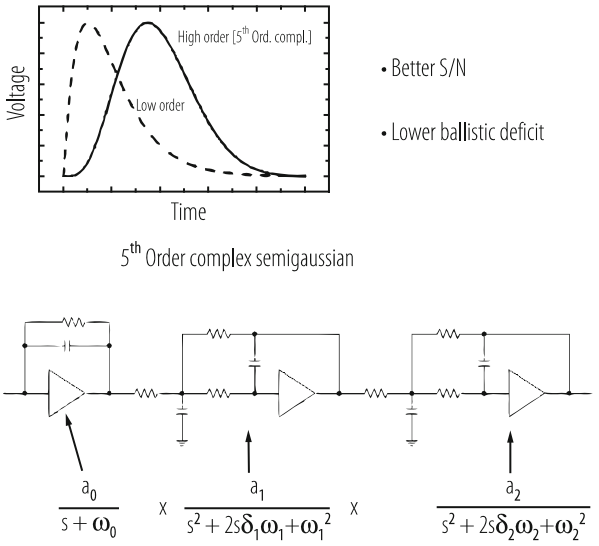

Fig. 10.23 A typical time-invariant signal processing chain resulting in a fifth order pseudo-Gaussian impulse response (weighting function), where s is the Laplace transform variable. This function results in lower noise coefficients A_1, A_2, A_3, Eqs. (10.6, 10.7, and 10.8), 2.2, 1.05, and 0.78, respectively, compared to a low-order CR-RC function *of equal width at the base*. See Ref. [10] for design considerations and other implementations

10.6.2 Uncorrelated Sampling and Digital Filtering

Sampled data digital signal processing has become prevalent in detector systems for gamma-ray and x-ray spectroscopy, for time projection chambers and in various forms in particle physics. One of the advantages is that it provides flexibility in the realization of mathematically optimal weighting functions. Optimal signal processing cannot be achieved without some analogue functions. An anti-aliasing filter is an essential part of the system. Its function is to limit the bandwidth prior to sampling so as to satisfy the Nyquist-Shannon sampling criterion: the bandwidth at the output of this filter must be no more than one half of the sampling frequency (the "Nyquist limit"). If this is not satisfied, the noise at frequencies higher than the Nyquist limit is shifted in frequency, i.e., ("aliased") by undersampling, to the frequencies below this limit. *The resulting loss in S/N due to aliasing cannot be recovered by any subsequent processing.* The role of digital filtering is to create optimized weighting functions in spectroscopic systems, and to enable an optimal particle track measurement in tracking systems. In spite of the power of digital processing, it is most efficient to cancel any long tails in the detector-preamplifier response by analogue means. If the tail cancellation is performed digitally, much larger numbers of samples have to be processed (deconvolved) for each event. For asynchronous (uncorrelated) sampling in semiconductor detectors for gamma-ray and x-ray spectroscopy see Refs. [37, 38]. In such systems optimum weighting functions are of trapezoidal form as in Fig. 10.19, where the flat top allows uniform weighting for a variable charge collection time.

10.6.3 Correlated Sampling

Correlated double sampling (CDS) is being used with many detectors in various implementations and under different names. One of these is known as "baseline subtraction"—taking a sample prior to the arrival of the usually unipolar signal (a delayed signal or with the arrival time known). This case is illustrated in Fig. 10.16, and it results in a bipolar weighting function, which defines quantitatively the effect of CDS on the noise, as discussed in Sects. 10.4.2 and 10.4.3. Correlated double sampling is an essential part of CCD signal processing in astronomy.

Signal processing by *multiple correlated (synchronous) sampling* has been used for noble liquid calorimeters, such as the liquid argon electromagnetic calorimeter in the ATLAS experiment, Refs. [39, 40].

10.7 Equipartition and *kTC* Noise

Integration of the power spectrum (spectral density) arising on a capacitance from the thermal noise current, $i_n^2 = 4kT/R$, of the resistor results in the *total fluctuation* of charge (and voltage), which is *independent of the value of the resistance R*. The bandwidth (equivalent to an abrupt cutoff) of the RC circuit in Fig. 10.24 is 1/(4*RC*), and the total fluctuation in voltage and charge is

$$\begin{aligned} \sigma_v^2 &= kT/C, \\ \sigma_q^2 &= kTC. \end{aligned} \tag{10.30}$$

The resistance (with the capacitance *C*) determines the bandwidth of the noise but not its magnitude. The *kTC* noise at 300 K is quite high even on small capacitances, as shown in Table 10.1. Most of this noise does not affect the measurement in systems where filtering and a very high parallel (feedback) resistance is used following a preamplifier, in other words where the noise corner time constant, Eq. (10.9), is much longer than the width of the filter weighting function. Such a system responds only to the portion of the spectrum where the spectral density is very low. *An example*: high resolution x-ray spectrometry with silicon detectors, where time-invariant or digital filtering is usually used. In contrast, when the measurement is performed by taking a sample directly on the detector capacitance and the filtering is not possible, the full *kTC* noise is included in the measurement, and it can be reduced only by correlated double sampling (CDS)—if applicable, as discussed in Fig. 10.27. CDS is just another way of excluding the noise at low frequencies from the measurement.

From the above discussion, which is based on circuit analysis, one is led to conclude that the *kTC* noise arises from the resistance, and yet its magnitude is independent of the value of the resistance. One may also be led to conclude that an "ideal" capacitance would have no noise. This is contradicted by the equipartition theorem which makes no direct assumption about the resistance. The equipartition

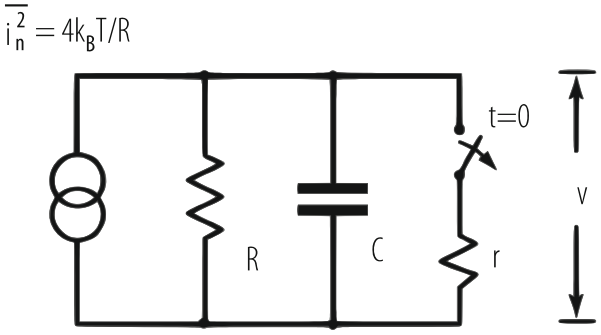

Fig. 10.24 A simple circuit for calculation of *kTC* noise

Table 10.1 Charge and voltage total fluctuation vs capacitance ($T = 300$ K)

Capacitance	Charge fluctuation	Voltage fluctuation
C [F]	$(kTC)^{1/2}/q_e$ [rms e]	$(kT/C)^{1/2}$ [μV]
1a	0.4	$6.4{\cdot}10^4$
10a	1.26	$2.0{\cdot}10^4$
100a	4	$6.4{\cdot}10^3$
1f	$1.26{\cdot}10$	$2.0{\cdot}10^3$
10f	$4.0{\cdot}10$	$6.4{\cdot}10^2$
100f	$1.26{\cdot}10^2$	$2.0{\cdot}10^2$
1p	$4.0{\cdot}10^2$	64
10p	$1.26{\cdot}10^3$	20
100p	$4{\cdot}10^3$	6.4

theorem states, that for a system in thermal equilibrium, the fluctuation energy per degree of freedom is *kT/2*. "*Per degree of freedom*" applies to any variable by which the energy of an energy storage object, or energy storage mode, can be defined. Thus for a capacitance, $C\langle v^2\rangle = kT/2$, from which Eq. (10.30) follows. So the statistical mechanics gives the same result for the total fluctuation but without any details about the dissipative components and the noise spectrum. A practical consequence is that as a capacitor becomes closer to an ideal one, the noise spectrum shifts toward zero frequency, while the total fluctuation remains constant.

We add here parenthetically that in a resonant system (an inductance- capacitance circuit), where there are two degrees of freedom, the noise spectrum is concentrated around the resonant frequency, while the integral of the power spectral density (total charge fluctuation) on the capacitance equals *kTC,* and the total current fluctuation (variance) in the inductance equals *kT/L*.

The above considerations apply also to analogous mechanical systems.

Transient behaviour of *kTC* noise is of great interest for switched capacitance circuits and for pixel detectors, where pixels are read out directly without filtering, by being sampled in a matrix arrangement, either before or after simple amplifiers (source followers, or three transistor circuits as in, Figs. 10.32, 10.33, and 10.34).

Transient behaviour of noise on a capacitance after switching the resistance or capacitance can best be studied by applying Campbell's theorem, as shown in Figs. 10.25 and 10.26. In this case the integration of the variance has to be carried out from the time when the switching takes place (zero) to the time t when the observation is made,

$$\sigma_v^2 = \left(\frac{1}{2}\right) 4kT \frac{1}{R} \int_0^t h^2(u)du = \frac{kT}{C}\left(1 - \mathrm{e}^{-2t/\tau}\right). \tag{10.31}$$

The oscillogram shows build-up of noise after switching a white noise source onto an RC circuit, $h(t) = (1/C)\mathrm{e}^{-t/\tau}$. The time constant τ equals the product of the capacitance and the resistance after the switching. Such a build up occurs after

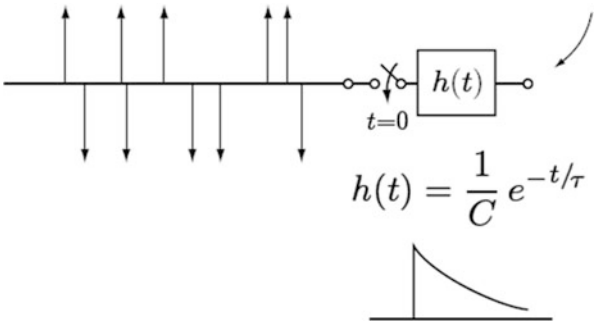

Fig. 10.25 Model for calculation of the build-up of *kTC* noise on an RC circuit

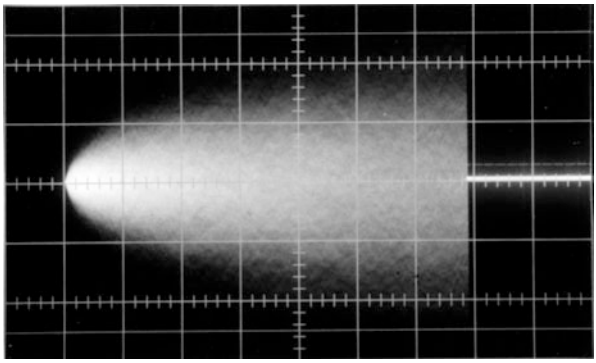

Fig. 10.26 Build-up of kTC noise on an RC circuit

a reset switch across a capacitor is opened and a much higher value of resistance appears in parallel with the capacitance. This is illustrated in Fig. 10.27.

Figure 10.27 illustrates what happens with *kTC* noise in active pixel sensors and CCDs. While the reset switch is closed, the *kTC* noise extends to very high frequencies corresponding to the very short time constant $r_{ON}C$. When the switch is "opened" the time constant increases by many orders of magnitude. A value of the "*old*" *kTC* noise is stored on the capacitance, and it decays very slowly with this very long time constant, CR_{OFF}. It is this sample of the "*old*" wide bandwidth noise that is often referred to as the "*reset noise*", even though its origin is not in the reset action. During the same time after switching, the "*new*" *kTC* noise builds up also very slowly, but faster than the stored value decays, since the rms noise build-up proceeds as $(1 - \exp[-2\, t/CR_{OFF}])^{1/2}$, Eq. (10.31) and Fig. 10.27. From this illustration one can see the conditions under which correlated double sampling may reduce significantly the *kTC* noise: *Sample 1 may be taken any time between opening of the reset switch and the arrival of the signal. Sample 2 may be taken any time after the arrival of the signal but before the "new" kTC noise has built up.*

Analysis of the effects of the *kTC* noise in some cases is not straightforward. Here are some general guidelines:

- *Fluctuation-dissipation theorem* with Johnson-Nyquist expression for thermal noise is essential for calculation of noise spectra and for detailed information on noise sources based on circuit analysis.

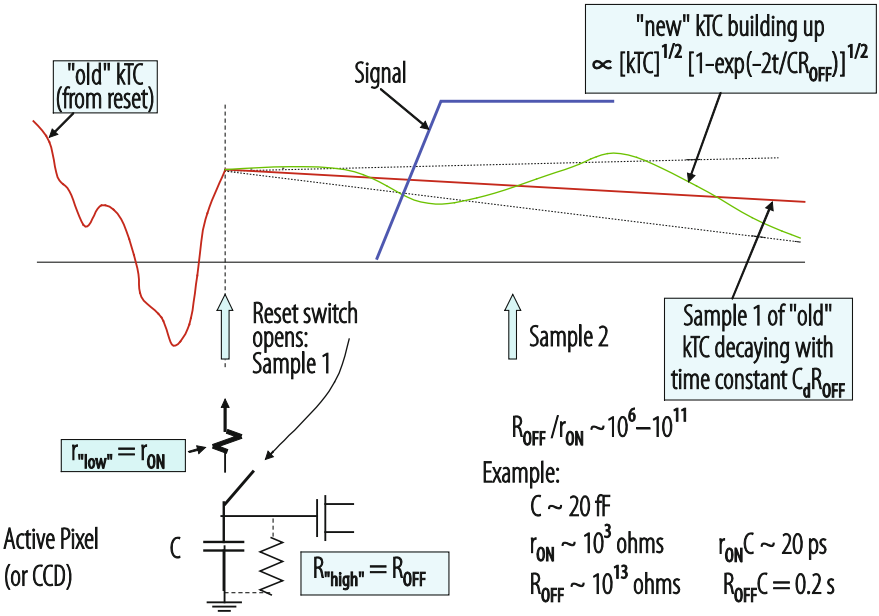

Fig. 10.27 Transient behaviour of *kTC* noise caused by the reset action of the sense node in CCDs and in pixel detectors with matrix readout (e.g., hybrid CMOS detectors)

- *Equipartition theorem* provides no detailed information on the noise spectra, but provides a *check on the integrals* of noise spectra (the total fluctuation).
- *Transient behaviour* of noise in switched capacitor circuits and matrix readout pixel arrays is best understood by means of *Campbell's theorem*, which provides *noise variance vs time*, as shown in Figs. 10.25, 10.26, and 10.27 and by Eq. (10.31). The knowledge of the dissipative component (resistance) is necessary for the transient analysis.
- A charge reset and transfer by a switch result in *kTC* independently of the switch ON resistance. This noise can be subtracted only if the *first sample* in the CDS is taken *before the signal*.
- Transfer (i.e., direct transport) of charge without switching (as in a CCD) does not result in *kTC* noise. *Reset* of the sense node *does*.

A frequently asked question: Can the total charge fluctuation (variance) on a capacitance be reduced below *kTC*? Yes, by "electronic cooling", where the apparent noise temperature of the resistance in parallel with the capacitance is reduced by feedback, Sect. 10.8.1 and Ref. [45]. While this is useful in practice, a note should be made that a system with active elements (gain) cannot be considered as being in thermal equilibrium with the surrounding.

An important distinction between two classes of signal processing schemes should be emphasized: (1) when no filtering (band limiting) takes place before the measurement, the total *kTC* fluctuation will contribute fully to the charge

measurement, and usually plays a dominant role. In contrast, (2) with charge amplifiers followed by filtering, the contribution of this noise (then usually referred to as "parallel noise") can be made negligible in most cases, by avoiding the low frequency part of the spectrum (by using a short peaking time, Fig. 10.14). Correlated double sampling (CDS) is one form of filtering.

10.8 Some Basic Signal Processing and Detector Readout Circuits

10.8.1 Charge Amplifier Configuration

In the most basic charge amplifier feedback configuration only two transistors are essential to realize a complementary cascode, as shown in Fig. 10.28. The current sources in positive and negative supplies can be realized by resistors or by low noise transistor current sources. There is only one significant pole (C_0R_0) in the first order solution for the response of this circuit. Higher order poles are given by the unity gain frequency of the transistors used. The cascode alone is an "operational transconductance amplifier" (very high output impedance). With the follower amplifier $\times 1$ it becomes an operational amplifier.

Gain and input impedance relations for the feedback charge amplifier configuration are derived from Figs. 10.28 and 10.29. The frequency dependence of the open loop gain is inherent to a high gain single pole amplifier. It is described by two parameters, unity gain frequency $\omega_h = g_m/C_0$, and the gain "roll off" frequency (3 dB point) $\omega_l = 1/(R_0C_0)$. The dc gain is then $|G_0| = \omega_h/\omega_l = g_m/R_0$, where g_m is the transconductance of the input transistor, C_0 is the dominant pole capacitance and R_0 is the dominant pole resistance. Input impedance with capacitive feedback has two terms, a resistance $R_{in} = 1/\omega_h C_f$ in series with a capacitance C_f G_0. The resistance term R_{in}, in conjunction with the total input capacitance, determines the

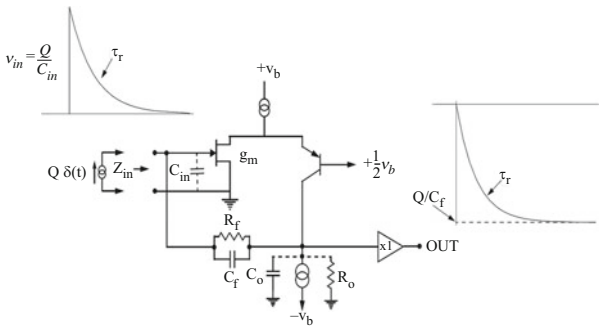

Fig. 10.28 Basic folded cascode charge amplifier feedback configuration

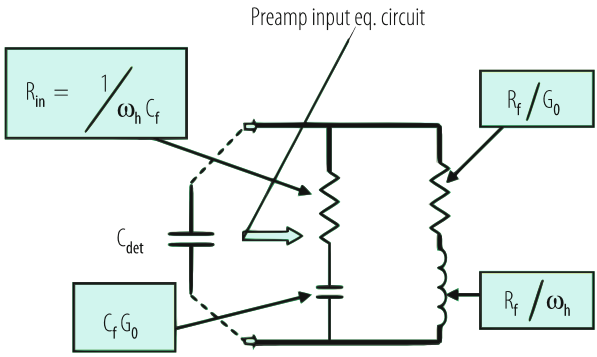

Fig. 10.29 Input equivalent circuit of feedback charge amplifier

rise time of the detector-amplifier. The rise time constant of the output voltage (i.e., the transfer of charge from the detector capacitance to the feedback capacitance) is $\tau_r = R_{in}C_{in} = (1/\omega_h)(C_{in}/C_f) = (C_0/g_m)(C_{in}/C_f)$, where $C_{in} = C_{det} + C_{ampl}$.

The resistive input impedance has a noise corresponding to the amplifier series noise resistance R_{seq}, and it appears as a resistance with a noise temperature, $T_{\text{eff}} = TR_{seq}/R_{in}$. For values of R_{in} higher than R_{seq}, the amplifier can be used as a termination for delay lines with a noise lower than that of a termination with a physical resistor Z_0 at temperature T.

The apparent noise temperature of the resistance Z_0 realized by the capacitance in feedback is $TR_{seq}/Z_{0,}$ and this is why it can be called "electronically cooled termination" or "electronically cooled damping", Ref. [45]. The resistance in parallel with the feedback capacitance adds two more terms to the input impedance of the preamplifier: inductance R_f /ω_h in series with a resistance R_f/G_0. It is important to note the condition to achieve an aperiodic ("damped") response of the feedback amplifier.

The feedback configuration allows the ultimate in noise performance because the parallel noise sources can be made negligible by using a transistor with a very low gate leakage current and a very high feedback resistance (megaohms to gigaohms). The feedback resistor can be avoided altogether by the use of optoelectronic feedback or a transistor switch to maintain amplifier voltages in the operating range. Signal integration is performed on the feedback capacitance C_f. The long tail can be cancelled in subsequent pulse shaping by a simple pole-zero cancellation circuit (not shown in the figure). Pulse shaping at the preamplifier by reducing R_L or R_f would result in increased noise from the thermal noise of these resistors. The object of the design is to avoid dissipative components at the detector-amplifier input and thus to make R_f as large as possible.

10.8.2 Cascaded Charge Amplifier Chain with Pole-Zero Cancellation

While the basic charge amplifier concept of a simple cascode circuit with a single dominant pole and capacitive feedback has not changed since the days of vacuum tube technology, the charge restoration techniques to control the operating point of the input transistor have evolved, particularly with the advent and widespread application of CMOS monolithic circuit technology. The dc feedback in charge amplifiers via a resistor (R_f in Fig. 10.28) has always been a problem in applications striving to achieve the ultimate in noise performance. Very high values in the gigaohm range are required in x-ray and gamma-ray spectroscopy, as this resistor injects a noise current inversely proportional to this resistance directly into the input node (i.e., "parallel noise", Sect. 10.4.5). In most applications the resistance values required are higher than the practical range of polysilicon resistors in CMOS technology. In some applications where the detector capacitance is very low it is best to avoid entirely any resistor and any continuous dc feedback. Various charge restoration techniques using switching or "reset" have been developed. An example is the CCD readout as shown in Fig. 10.35.

Continuous charge restoration is usually simpler to implement and better suited in many applications where its noise contribution is negligible, i.e., with higher detector capacitances and shorter weighting functions (peaking times). Most present gas, noble liquid and silicon particle detectors fall into that category. Additional considerations in the choice between switched and continuous charge restoration are the knowledge of the event arrival time and whether switching transients pose a problem. Continuous feedback in MOS technology is realized by a transistor with a long and narrow channel (L»W). The resistance of such a device will depend on the signal amplitude and on the detector leakage resulting in a nonlinear response. An elegant solution for accurate nonlinearity compensation is shown in Fig. 10.30. The transistor-capacitor network between the two amplifiers is an exact replica of the feedback network but increased in width by a factor *N*. Both networks operate at equal voltages on the two transistors and this ensures the compensation of

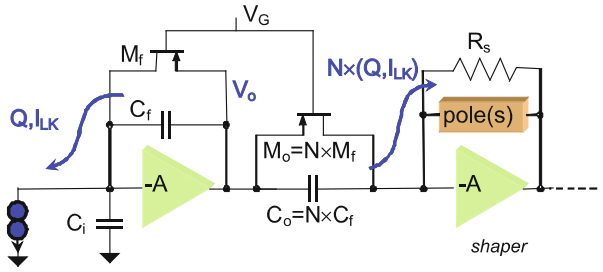

Fig. 10.30 Charge amplifier with continuous reset, pole-zero cancellation and compensation of non-linearity in the feedback transistor [10, 46]

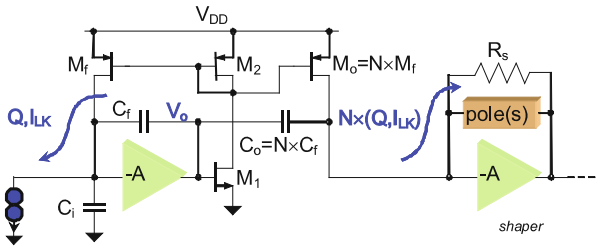

Fig. 10.31 An alternative configuration for a charge amplifier with pole-zero and transistor nonlinearity compensation [10]

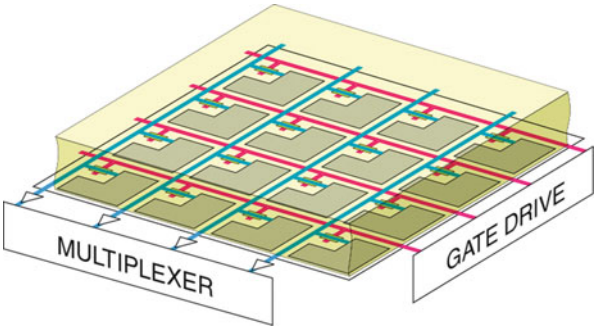

Fig. 10.32 Matrix readout of integrating pixel detectors. Transistors switches are integrated on the detector substrate

nonlinearity and pole-zero cancellation. The charge (current) gain in the first stage including the pole-zero network equals *N*.

An alternative configuration is shown in Fig. 10.31. An advantage of this configuration is that it separates the bias point of the transistors M_f and M_o from the virtual ground of the amplifiers. This results in a larger dynamic range. The configuration in Fig. 10.31 can be used as an input stage (charge amplifier) or as a second stage where several gain stages are needed. An analysis of both configurations is given in Ref. [10, 70, 71]. An overview of dc charge restoration circuits is given in Ref. [47].

10.8.3 Pixel Matrix Readout

Large pixel arrays can be conveniently read out by a matrix arrangement as illustrated in Fig. 10.32. The charge due to a photon or charged particle is stored on a pixel capacitance. The switches (one/pixel) connect a row of pixels to charge amplifiers located at the bottom of the columns. In this way, a multiplexing density is achieved between that for a separate readout for each pixel and the CCD with only

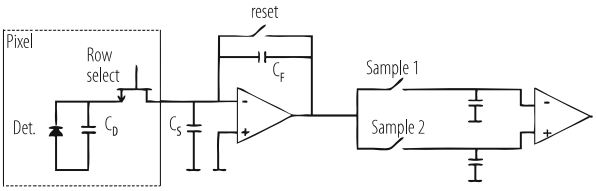

Fig. 10.33 Basic circuit diagram of the matrix readout with a switch (and no amplification) in each pixel [41–43]

one readout for the entire array. Such an array can be used in single event counting mode at sufficiently low event rates, or in charge integrating mode at very high event rates. This type of readout allows the use of the same technology, or different technologies, for the detector and the switching transistors. For many applications this approach is the best compromise between interconnect complexity and the speed of readout. An example of such an imaging detector for x-ray radiography is described in Ref. [41], and a silicon detector with Junction FET switches in Ref. [42]. The equivalent circuit diagram of such a readout with correlated double sampling is given in Fig. 10.33. It is convenient to group the noise contributions in this case in two classes: those that can be reduced by correlated double sampling and those that cannot. Referring to the notation in Fig. 10.33, the former are the reset (kTC) noise of capacitances C_f and C_s, and the latter are the reset noise of the charge collecting pixel C_d, shot noise from pixel dark current and amplifier series white noise. The reset (kTC) noise on the pixel capacitance C_d cannot be reduced by double correlated sampling according to the discussion in Sect. 10.7 and as illustrated in Fig. 10.27, because *both* the signal and the kTC noise start building up after the charge transfer from the pixel to the charge amplifier. Thus for the simplest matrix readout the minimum noise is limited by the pixel capacitance, Table 10.1, e.g., ~ 400 electrons rms for C_d ~ 1 pF at 300 K. There will also be a significant contribution by the amplifier noise if the connection capacitance along the column to the amplifier is large due to the size of the pixel array.

A much lower noise can be achieved in pixel arrays with "amplified pixels" as illustrated in Fig. 10.34. Each pixel has three or more transistors to perform the basic functions of reset, amplification and row selection. A CMOS matrix readout die can be bump-bonded (or in the future, directly bonded) to a pixel detector, or serve as a monolithic active pixel sensor (MAPS), Ref. [44]. Performing the reset in each pixel separately from the charge transfer (unlike in the simplest matrix readout without in-pixel amplification) allows almost complete cancellation of the pixel kTC noise by double correlated sampling, in applications where the time interval between the two samples is not too long (see Fig. 10.27). Noise levels in the range of 10–20 electrons rms have been achieved with small pixels (20–30 fF). The same level of noise has been achieved with larger pixels (~1 pF) and more conventional charge amplifiers and pulse shaping [48]. A lower noise with silicon pixel detectors has been achieved by integration of a field effect transistor on the high resistivity

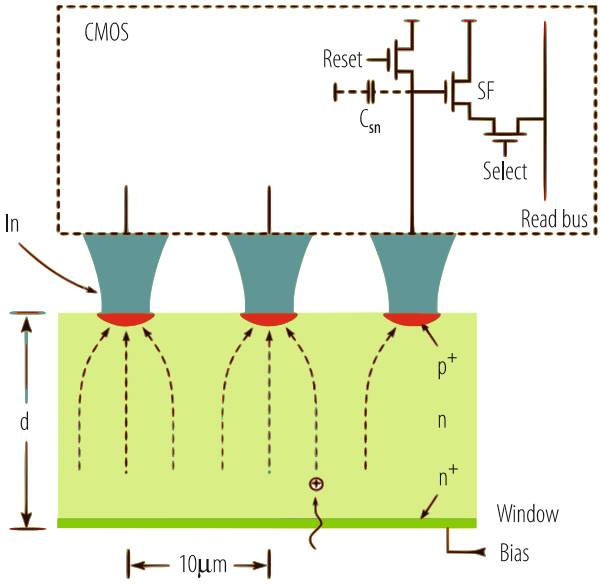

Fig. 10.34 Three transistor cell for readout of pixel detectors comprised of a source follower (SF), reset transistor switch and select transistor switch, illustrated for a bump-bonded hybrid detector. In monolithic active pixel CMOS detectors (MAPS), the readout cells are integrated with sensing diodes [44]. An overview is given in Ref. [43]

detector die (DEPFET, Ref. [49]). The lowest noise has been achieved with CCDs, Sect. 10.8.4. Each of these results was obtained after optimization for a particular application and each one involves a different set of parameters.

10.8.4 Charge Conserving (CCD) Readout

The charge coupled device (CCD), Fig. 10.35, is a device with the highest charge detection sensitivity among the photon and particle detectors. Low noise in the single electron rms range has been achieved [35, 69], thanks to a very low capacitance of the readout node and the integrated source follower (~15–30 fF), and the absence of any continuous conduction path to the sensing node. A switched reset is used after reading out the charge. Correlated double sampling is used to make the *kTC* noise negligible, as discussed in Sect. 10.7. Nearly complete *kTC* noise cancellation is achieved because the first sample is taken before the signal charge is transferred to the readout node (floating gate). Dual slope integration/trapezoidal weighting function is used for optimal filtering of the transistor (source follower) series noise, as discussed in Sect. 10.4.6.

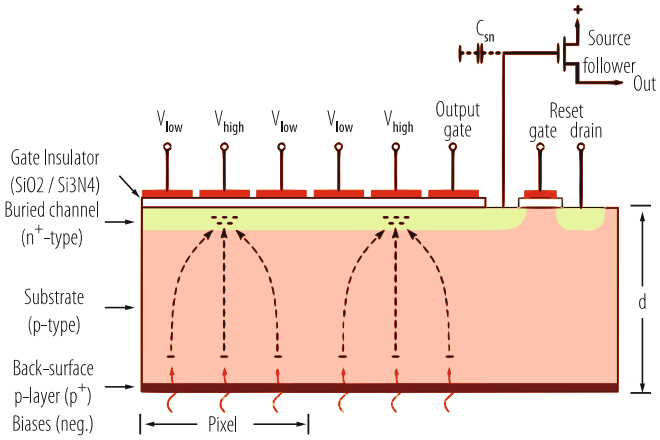

Fig. 10.35 An illustration of CCD read-out. The source follower (shown only schematically) is integrated on the CCD substrate as a buried channel enhancement mode MOSFET. The signal charge transferred from left to right is sensed at the floating electrode between the output gate and the reset gate. C_{sn} is the "node capacitance" = floating gate + gate to source capacitance of the transistor

10.9 Electronics Technology Outlook

10.9.1 Scaling of CMOS

The process of reduction of the size of CMOS transistors has continued for more than 40 years, and it is only very recently that it has started approaching fundamental physical limits. In this process the device is being scaled down in all three dimensions and in voltage, while the doping concentration is being increased. All dimensions are being reduced by a scaling factor α. This reduction includes all geometrical parameters of the device such as the gate oxide thickness t_{ox}, channel length L, channel width W, and junction depth. The substrate doping concentration is increased by the same scaling factor. The voltages applied were also expected to be reduced by the same scaling factor. These scaling rules were very clearly described in some detail already in 1974 [50], and the resulting device properties as a function of α are given in Table 10.2.

The scaling by a factor $\alpha = \sqrt{2}$ every ~2 years has followed the Moore's law [50] remarkably well until recently, with one exception. In the last few steps below the channel length $L \sim 0.13$ microns it is not possible to reduce the applied voltages by the same scaling factor. Downscaling has made the speed of the MOSFETs higher, the power dissipation per circuit lower, and it has enabled an ever-increasing level of integration (the number of transistors on a single chip). Aside from the enormous progress in all digital devices, it has made possible increasingly complex functions in the readout of detectors by integration of mixed signal (analogue and digital) circuits in Application Specific Integrated Circuits (ASICs).

Table 10.2 Scaling rules: dependence of device properties on scale factor α

Device property	Scaling rule
Electric field E	const.
Conductance (transconductance) $= I/V$	const.
Current density	const.
Power density	const.
Capacitance	$1/\alpha$
Speed $= I/CV = g_m/C = f_T$	α
Switching energy $= CV^2$	$1/\alpha^3$
Power/gate $= CV^2 f$	$1/\alpha^2$
Circuits density (transistors/unit area)	α^2

The principal impact on analogue ASICs has been:

- More, faster transistors
- Lower capacitance-lower noise readout of small detector pixels
- Better radiation resistance
- Prospects for vertical integration with high resistivity silicon detectors

However, the impact on analogue circuits has been very positive only up to a certain point of scaling. Scaling of CMOS into the deep submicron range (below 100 nm down to a few nm) has some undesirable consequences for low noise amplifier design:

- The low supply voltage "headroom" in scaled CMOS processes imposes limits on analogue circuit topologies. The increasing ratio of *VTH/VDD* rules out the use of many classical analogue design topologies.
- The *cascode connection*, useful in providing high gain loads and current sources, becomes difficult to realize once *VDD* falls below ~1.2 V.
- The electrostatic control of the channel by the gate is reduced, resulting in reduced ratio *Idon/Idoff*. In CMOS transmission gates, commonly found in sample/hold and switched capacitor circuits, self-discharge rates increase due to incomplete current cutoff.
- The reduced electrostatic control of the channel results also in a lower ratio of the drain conductance and the transconductance, i.e., the gain of the transistor. To achieve a certain gain more amplification stages may be needed.
- The dynamic range of capacitance based circuits, memories and sample & hold circuits, is reduced (the ratio of stored charge to the kTC noise), both due to the reduced V_{dd} and due to a lower storage capacitance.
- Gate tunneling current arising with thin oxides contributes shot noise.

While the scaling in the CMOS technology is driven by the entire information technology industry, some applications require higher operating voltages than dictated by the smallest feature sizes. This has been recognized, and the large semiconductor foundries offer options with a thicker gate oxide in their deep submicron platforms. For example, a nominal gate oxide thickness in the 65 nm platform (or "node") is about 65/50 $\approx$ 1.2 nm, but the process includes also on the

same wafer an oxide thickness of ~5 nm, that requires a minimum channel length of ~250 nm and allows a supply voltage of ~2.5 V. This will make possible in a single ASIC both high density digital circuits with the minimum feature size, and higher voltage input/output circuits and precision analogue circuits with an effectively larger feature size.

Analog design below 100 nm becomes gradually more difficult. The complexity of ASIC design rules and the costs of the design tools increase steeply as the feature size is reduced. This is discussed in some detail in Ref. [51].

While the developments in electronics technology have already made possible very large and complex detectors, the power dissipation associated with increasingly complex signal and data processing has been a problem and will remain a principal limitation and challenge.

Along with the quest in the CMOS scaling continuing down to the nodes in the ~7 to 28 nm range, an additional path to higher circuit densities and to higher speed of digital circuits (by shortening the interconnections) is three-dimensional integration of several thin layers of CMOS circuits [52, 53]. A significant breakthrough in particle and photon silicon detectors will be integration (by direct bonding) of a thick (50–500 μm) high resistivity p-i-n detector die to one or more thin (~10 μm) CMOS layers of readout electronics.

10.9.2 Transistors at Low Temperatures: Applications in Future Detectors

Most of the electronics for particle detectors has been based on silicon CMOS devices following the trends in electronics industry. Over the last two decades the technology of silicon–germanium heterojunction bipolar transistors (SiGe HBT) has been developed [54]. These devices have some key properties superior to the bipolar junction transistor (BJT), notably a much higher current gain and a much higher unity-gain frequency. The HBT, unlike the BJT can operate at liquid nitrogen temperature, and furthermore, with an increased current gain. Recently emerging cryogenic applications have generated renewed interest in low temperature properties of both CMOS and HBT technologies [54, 55]. As with HBTs, it has been found that various CMOS device properties improve at low temperatures. The mobility and the transconductance increase by a factor of two to three as the temperature decreases from 300 K to 43 K, and the (inverse) subthreshold slope decreases from ~90 mV/decade to ~20 mV/decade resulting in a higher ratio of the transconductance to the drain current. The transistor (series) thermal noise has been observed to decrease monotonically from 300 K to 40 K [56]. There is one *caveat*: CMOS transistors have to be operated (at any temperature) under conditions where hot electron generation, which is more pronounced at low temperatures, is minimized [57].

In particle physics, recently developed cold monolithic electronics has enabled scaling up of liquid argon time projection chambers to a very large size, required for studies of neutrino oscillations and nucleon decay. Such detectors, which originated with the ICARUS project [58], in the size range of up to few hundred tons, will have to be built in the range, unthinkable so far, of tens of kilotons. The number of sense electrodes (wires) and the readout amplifiers will be in the range of ~$5 \cdot 10^5$ to $3 \cdot 10^6$, assuming a reasonable electron drift length in the time projection chamber (TPC) and the sense wire length. Readout by monolithic amplifiers (with multiplexing) placed at wire electrode frames, results in a significantly lower noise (due to a lower capacitance) than with long cables bringing the signals from each sense wire to the outside of the cryostat, and in a much lower number of cables and feedthroughs. This also allows the design of the cryostat to be freed from the signal cable constraints. The "cold electronics" in this case will have a beneficial impact on both the engineering and the physics, i.e., a higher signal-to-noise ratio allowing better background rejection and a higher precision in the track measurement and reconstruction increasing the sensitivity for detection of interesting phenomena [59, 60]. Such a detector, on a smaller scale (~75 tons of liquid argon with ~8300 sense wires and electronic channels immersed in liquid argon), has been built and operated for two years. Uniformity and stability of the gain and noise has been demonstrated [61].

10.9.3 Beyond the Moore's Law

As the MOSFET technology advances further into the nanoscale domain (gate widths down to 5–10 nm), Moore's law, as defined for CMOS transistors, is running up against the physical, technical and economical limitations, and eventually against the granularity of matter (silicon lattice constant ~0.54 nm). Physical phenomena associated with small dimensions, such as quantum mechanical effects and fluctuations in the decreasing number of dopants, take place. These effects cause leakage currents (incomplete drain current turn-off and gate tunnelling currents) and dispersion in device parameters (threshold voltage). Associated with the necessity for tighter control of all device and fabrication process parameters are increasing costs.

Recent research toward smaller, faster and lower power devices has been concentrated on "beyond CMOS" devices [62–64]. As with the CMOS, new developments are being driven by the needs for high density-high speed digital and computer circuits. Besides the physical variables considered as "computational variables" familiar in CMOS (current, voltage, charge), other variables are being considered (electric dipole, magnetic dipole, orbital state). Among possible device concepts being explored are:

- Tunneling FET
- Graphene nanoribbon FET

- Bilayer pseudo spin FET
- SpinFET
- Spin transfer torque/domain wall
- Spin torque oscillator logic
- All spin logic device
- Spin wave device
- Nanomagnet logic
- III–V tunnel FETs

Each of these devices may have some properties superior to CMOS, but none, so far, satisfies the set of simple criteria that CMOS does. For example, upon analysis, the spintronic devices have longer switching delays and higher switching energies, due to inherent time of magnetization propagation.

Any "Beyond CMOS" device should have many of the same characteristics as CMOS devices:

- Power gain >1
- Ideal signal restoration and fan-out (output of one device can drive two or more devices)
- Feedback prevention (output does not affect input)
- High ON/OFF current ratio ~ $10^{5–7}$
- Low static power dissipation
- Compatibility with Si CMOS devices for mixed functions

The consensus about the future technology has been so far: No new device is yet on the horizon with a potential to completely replace CMOS. More likely, new devices may emerge by gradual evolution. New or special functions (e.g., memories, [34]) may become possible in the nanoscale devices by new physics and such devices may be merged into CMOS circuits to enhance overall performance. Impedance matching may be necessary from the quantum resistance values (kohms) down to the 50–100 ohm range. The overall logic operations and communications will still be based on CMOS. Future integrated circuits are likely to still contain a majority of CMOS devices with a few other beyond-CMOS devices performing various specialized functions. An in depth evaluation of the various device concepts under investigation is given in Ref. [65, 72].

Work on carbon nanotubes as active electronic devices and passive devices (interconnects) has been going on for the last three decades. Some interesting devices and phenomena have been described extensively in literature [64]. Carbon nanotube as a channel in an MOS transistor structure has higher mobility, reducing electron transit time. However, accurate placement of carbon tubes, and the need to form higher current channels by placing multiple carbon tubes in parallel, has been a challenge to fabricate uniform devices. Graphene based devices are analyzed in Ref [66].

In the quest for nanoscale devices and higher density of analogue and digital functions other limitations appear. Since all logic circuits (even spintronics circuits)

need electrical contacts at the terminals of gates and channels (source and drain) their size will be limited by the metallization dimensions.

As far as particle and photon detectors are concerned, further progress in digital circuit technology, based on nanoscale nodes, will result in increased functionality of the detector circuits, particularly those integrated with detectors, as long as they are economically available from multi-project foundry services or as commercial components. The development of multi-layer (3D) circuits for detectors has been challenged by limited access to this technology, given the relatively small quantities needed in physics experiments and high costs.

As far as the analogue front-end circuits for particle detectors are concerned, it appears that CMOS will be less useful below the ~65 nm node (Sect. 10.9.1 and Ref. [51]). In higher precision circuits, such as analogue to digital converters and switched capacitor memories, the dynamic range is limited by the low power supply voltages (one volt or less) at the upper end and by the *kTC* noise at the lower end. Fortunately. the provision of thicker oxide devices on the same nanoscale platforms leaves the choice of the operating voltage, the gate length and width to the designer (as discussed in Sect. 10.9.1).

An interesting domain, outside of the CMOS mainstream, has been presented by *single-electron transistors* (SETs), [67, 68]. Single electron transistors are devices with a capacitance so small that a single electron can generate a measurable voltage (above the thermal voltage). To be observable, the mean energy of the electron on the capacitance must be several times larger than its thermal energy (*kTC* noise). This sets an upper limit on the capacitance of the control electrode (gate) of the transistor (and the sensor connected to the transistor) and on the operating temperature. From Sect. 10.7 and Table 10.1, an upper limit for the capacitance at room temperature would be 1 aF (10^{-18} F). Alternatively, the temperature would have to be 300 mK, to allow a capacitance in the range of ~1 fF. SETs, although known for more than three decades, have not been considered suitable for integration due to large variability in their fabrication.

SETs might be suitable as very sensitive electrometers for *equally low capacitance* sensors. That sensitivity is for the most part due to their low capacitance and in part due to improved carrier transport properties. At 300 K they are not matched to even the smallest pixels of present particle and photon detectors, and will be useful only with an entirely new generation of very fine grained detectors operated at low temperatures.

Acknowledgments The author is indebted to his colleagues, Gianluigi De Geronimo, Paul O'Connor, Sergio Rescia, Bo Yu, and the late Pavel Rehak for many stimulating discussions and, over time, for contributions of material that has contributed greatly to this article. In particular, most of the induced signal simulations are due to Bo Yu, the circuits shown in Figs. 10.23, 10.30 and 10.31 originated in publications by Gianluigi De Geronimo and Paul O'Connor. Paul O'Connor provided much of the material on CMOS scaling, and Sergio Rescia worked with the author on *1/f* and *kTC* noise calculations. Special thanks are to Anand Kandasamy for help with editing of the manuscript and the figures.

References

1. G. Knoll, *Radiation Detection and Measurement*, John Wiley & Sons (2000).
2. C. Grupen and B. Shwartz, *Particle Detectors*, 2nd edition, Cambridge University Press (2009).
3. G. Lutz, *Semiconductor Radiation Detectors*, Springer-Verlag (1999).
4. H. Spieler, *Semiconductor Detector Systems*, Oxford University Press (2005).
5. I. Iniewski (ed.), *Medical Imaging*, John Wiley & Sons (2009).
6. D.M. Binkley, *Tradeoffs and Optimization in Analog CMOS Design*, John Wiley & Sons (2008).
7. C.C. Enz, E.A. Vittoz, *Charge-based MOS Transistor Modeling*, John Wiley & Sons (2006).
8. E. Gatti, P.F. Manfredi, *Processing the Signals from Solid-State Detectors in Elementary Particle Physics*, Rivista de Nuovo Cimento, 9(1) (1986).
9. V. Radeka, *Low-Noise Techniques in Detectors*, Annu. Rev. Nucl. Part. Sci. 38 (1988) 217.
10. G. De Geronimo, *Low-Noise Electronics for Radiation Sensors*. In: Medical Imaging, K. Iniewski (ed.), John Wiley & Sons (2009) p. 127.
11. W. Shockley, *Currents to Conductors Induced by a Moving Charge*, J. Appl. Phys. 9 (Oct. 1938) 635.
12. S. Ramo, *Currents Induced by Electron Motion*, Proc. IRE 27(1939) 584-585.
13. E. Gatti, G. Padovini, V. Radeka, *Signal Evaluation in Multielectrode Detectors by Means of a Time Dependent Weighting Vector*, Nucl. Instrum. Meth. 193 (1982) 651.
14. N.R. Campbell, *Proc. Cambridge Philos. Soc.* 15 (1909) 117.
15. P.N. Luke, *Unipolar Charge Sensing with Coplanar Electrodes – Application to Semiconductor Detectors*, IEEE Trans. Nucl. Sci. 42 (1995) 207.
16. V. Radeka, *1/|f|Noise in Physical Measurements*, IEEE Trans. Nucl. Sci. NS-16 (1969) 17.
17. C.M. Compagnoni et al., *Statistical Model for Random Telegraph Noise in Flash Memories*, IEEE Trans. Electron Devices 55(1) (2008) 388.
18. K. Kandiah, M.O. Deighton, F.B. Whiting, *A Physical Model for Random Telegraph Signal Currents in Semiconductor Devices*, J. Appl. Physics 86(2) (1989) 937.
19. P. van der Wel et al., *Modeling Random Telegraph Noise Under Switched Bias Conditions Using Cylostationary RTS Noise*, IEEE Trans. Electron Devices 50(5) (2003) 1378.
20. A. Konczakowska, J. Cicshosz, A. Szewczyk, *A New Method for RTS Noise of Semiconductor Devices Identification*, IEEE Trans. Instrum. Meas. 57(6) (2008) 1199.
21. L.K.J. Vandamme, F.N. Hooge, *What Do We Certainly Know About 1/f Noise in MOST?*, IEEE Trans. Electron Devices 55(11) (2008) 3070.
22. R. Wilson, *Noise in Ionization Chamber Pulse Amplifiers*, Philos. Mag., Ser. 7 Vol. xli, Jan. (1950) 66.
23. V. Radeka, *Optimum Signal Processing for Pulse Amplitude Spectrometry in the Presence of High-Rate Effects and Noise*, IEEE Trans. Nucl. Sci. NS-15 (1968) 455.
24. M. Konrad, *Detector Pulse Shaping for High Resolution Spectroscopy*, IEEE Trans. Nucl. Sci. NS-15 (1968) 268.
25. V. Radeka, *Trapezoidal Filtering of Signals from Large Germanium Detectors at High Rates*, Nucl. Instrum. Meth. 99 (1972) 535.
26. S. Rescia, V. Radeka, unpublished notes.
27. G.R. Hopkinson, D.H. Lumb, *Noise Reduction Techniques for CCD Image Sensors*, J. Phys. E: Sci. Instrum., 15 (1982) 1214.
28. E. Gatti et al., *Suboptimal Filtering of 1/f Noise in Detector Charge Measurements*, Nucl. Instrum. Meth. A 297 (1990) 467.
29. V. Radeka, *Semiconductor Position Sensitive Detectors*, Nucl. Instrum. Meth., 226 (1984) 209.
30. V. Radeka, *State of the Art of Low Noise Amplifiers for Semiconductor Radiation Detectors*, Proc. Int'l. Symposium on Nuclear Electronics, Versailles, 1968, Vol. 1 (1968) 46-1.
31. V. Radeka, *Field Effect Transistors for Charge Amplifiers*, IEEE Trans. Nucl. Sci. NS-20 (1973) 182; see also, V. Radeka, *The Field-Effect Transistor – Its Characteristics and Applications*, IEEE Trans. Nucl. Sci. NS-11 (1964) 358.

32. H.B. Callen, R.F. Greene, *On a Theorem of Irreversible Thermodynamics*, Phys. Rev. 86 (1952) 701.
33. H.B. Callen, T.A. Welton, *Irreversibility and Generalized Noise*, Phys. Rev. 83 (1951) 34.
34. D.B. Strukov, K.K. Likharev, *CMOL FPGA: A cell-Based, Reconfigurable Architecture for Hybrid Digital Circuits Using Two-Terminal Nanodevices*, Nanotechnology 16 (2005) 888.
35. R.P. Craft et al., *Soft X-ray Spectroscopy with Sub-Electron Readnoise Charge-Coupled Devices*, Nucl. Instrum. Meth., A 361 (1995) 372.
36. F.S. Goulding, D.A. Landis,, N.W. Madden, *Design Philosophy for High-Resolution Rate and Throughput Spectroscopy Systems*, IEEE Trans. Nucl. Sci. NS-30 (1983) 301.
37. V.T. Jordanov, G.F. Knoll, *Digital Synthesis of Pulse Shapes in Real Time for High Resolution Radiation Spectroscopy*, Nucl. Instrum. Meth. A 345 (1994) 337. X-ray Instrumentation Associates, *Appl. Note* 970323-1.
38. O. Benary et al., *Liquid Ionization Calorimetry with Time-Sampled Signals*, Nucl. Instrum. Meth. A 349 (1994) 367.
39. B.T. Turko, R.C. Smith, Conf. Record of the 1991 IEEE Nucl. Sci. Symp., (1991) 711.
40. O. Benary et al., *Precision Timing with Liquid Ionization Calorimeters*, Nucl. Instrum. Meth. A 332 (1993) 78.
41. N. Matsuura et al., *Digital Radiology Using Active Matrix Readout: Amplified Pixel Detector Array for Fluoroscopy*, Med. Phys. 26(5) (1999) 672.
42. W. Chen et al., *Active Pixel Sensors on High Resistivity Silicon and Their Readout*, IEEE Trans. Nucl. Sci. 49(3) (2002) 1006.
43. V. Radeka, *CCD and PIN-CMOS Developments for Large Optical Telescopes*, Proc. SNIC Symposium, Stanford, Ca., April 3–6, 2006.
44. G. Deptuch et al., *Monolithic Active Pixel Sensors with In-pixel Double Sampling Operation and Column-level Discrimination*, IEEE Trans. Nucl. Sci. 51(5) (2004) 2313.
45. V. Radeka, *Signal, Noise, and Resolution in Position-Sensitive Detectors*, IEEE Trans. Nucl. Sci. NS-21(1) (1974) 51.
46. G. De Geronimo, P. O'Connor, *A CMOS Fully Compensated Continuous Reset System* IEEE Trans. Nucl. Sci. 47 (2000) 1458.
47. G. De Geronimo et al., *Front-End Electronics for Imaging Detectors*, Nucl. Instrum. Meth. A 471 (2001) 192.
48. P. O'Connor et al., *Ultra Low Noise CMOS Preamplifier-Shaper For X-ray Spectroscopy*, Nucl. Instrum. Meth. A 409 (1998) 315.
49. J. Kemmer, G. Lutz, *New Semiconductor Detector Concepts*, Nucl. Instrum. Meth. A 253 (1987) 365.
50. R.H. Denard et al., *Design of Ion Implanted MOSFETs with Very Small Physical Dimensions*, J. Solid-State Circuits SC-9 (1974) 256.
51. L.L. Lewyn et al., *Analog Circuit Design in Nanoscale CMOS Technologies*, Proc. IEEE 97(10) (2009) 11687.
52. IBM J. Res. & Dev., Issue on *3D Chip technology*, 52(6) (2008).
53. Proc. IEEE, Issue on *3-D Integration*, 97(March) (2009).
54. J.D. Cressler, *On the Potential of SiGe HBTs for Extreme Environment Electronics*, Proc. IEEE 93(9) (2005) 1559.
55. T. Chen et al., *CMOS Reliability Issues for Emerging Cryogenic Lunar Electronics Applications*, Solid-State Electron. 50 (2006) 959.
56. G. De Geronimo et al., *Front-End ASIC for a Liquid Argon TPC*, IEEE Trans. Nucl. Sci., Vol. 58, No. 3, June (2011) 1376–1385.
57. S. Li et al., *LAr TPC Electronics CMOS Lifetime at 300 K and 77 K and Reliability Under Thermal Cycling*, IEEE Trans. Nucl. Sci. Vol. 60, No. 6, Dec. (2013) 4737–4743.
58. S. Amerio et al., *Design, Construction and Tests of the ICARUS T600 Detector*, Nucl. Instrum. Meth. A 527(2004) 329, and references therein.
59. V. Radeka et al.,*Cold Electronics for "Giant" Liquid Argon Time Projection Chambers*, Journal of Physics: Conference Series, Vol. 308, No. 1, (2011) 012021.
60. H. Chen et al.,*Cryogenic Readout Electronics R&D for MicroBooNE and Beyond*, Nucl. Instrum. & Meth. A 623 (2010) 391–393.

61. R. Acciarri et al., *Noise Characterization and Filtering in the MicroBooNE Liquid Argon TPC, JINST,* 12:P08003, 2017, 1705.07341.
62. T. Hiramoto et al., *Emerging Nanoscale Silicon devices Taking Advantage of Nanostructure Physics*, IBM J. Res. & Dev. 50(4/5) (2006) 411.
63. M. Haselman, S. Hauck, *The Future of Integrated circuits: A Survey of Nanoelectronics*, Proc. IEEE 98(1) (2010) 11.
64. Int. J. High Speed Electron. Syst., Issue on *Nanotubes and Nanowires*, 16(4) (2006).
65. D.E. Nikonov, JSNM 21, 497 (2008).
66. F. Schwierz, *Graphene Transistors: Status, Prospects, and Problems,* Proc. IEEE, 101(7) (2013) 1567.
67. D.D. Smith, *Single Electron Devices*, Int. J. High Speed Electron. Syst. 9(1) (1998) 165.
68. M.H. Devoret, R.J. Schoelkopf, *Amplifying Quantum Signals with the Single-Electron Transistor*, Nature 406(31 Aug) (2000) 1039.
69. R.P. Kraft et al., *Soft X-ray Spectroscopy with Sub-Electron Readnoise Charge-Coupled Devices*, Nucl. Instrum. Meth. A 361 (1995) 372.
70. G. De Geronimo, P. O'Connor, *A CMOS Detector Leakage Current Self-Adaptable Continuous Reset System: Theoretical Analysis*, Nucl. Instrum. Meth. A 421 (1999) 322.
71. P. O'Connor, G. De Geronimo, *Prospects for Charge Sensitive Amplifiers in Scaled CMOS*, Nucl. Instrum. Meth. A 480 (2002) 713.
72. D. E. Nikonov and I. A. Young, *Overview of Beyond-CMOS Devices and a Uniform Methodology for Their Benchmarking,* Proc. IEEE, 101(12) 2013.